



Continuum mechanics-based shell elements with six degrees of freedom at each node – the MITC4 / D and MITC4+ / D elements

Yeongbin Ko^{a,*}, Klaus-Jürgen Bathe^b, Xinwei Zhang^a

^a Bentley Systems, Incorporated, Team ADINA, 685 Stockton Drive, Exton, PA 19341, USA

^b Department of Mechanical Engineering, Massachusetts Institute of Technology, Cambridge, MA 02139, USA

ARTICLE INFO

Keywords:

Continuum-mechanics based shell finite elements
4-node elements
MITC method
Locking
Drill rotations
Numerical testing

ABSTRACT

We give the formulation and numerical assessment for using six degrees of freedom at each node of 4-node continuum mechanics-based quadrilateral shell elements. The formerly published MITC4 and MITC4+ shell elements are considered and extended to now include the drilling rotational degrees of freedom at the nodes. Including these degrees of freedom enables the modeling of shells with beam elements and shell surfaces intersecting at large angles and in addition results in an improvement of the membrane behavior of the elements. The elements pass all basic tests, show alleviated locking behavior in the analysis of general curved geometries and show close to optimal convergence behaviors in the analysis of the “all-encompassing” shell test problems.

1. Introduction

An effective numerical scheme to analyze shell structure is of high importance [1,2,3,4]. In finite element analysis, continuum mechanics-based shell finite elements have been widely adopted because these elements directly couple the membrane, shear and bending behaviors. The element behaviors are described using five degrees of freedom at the nodes. We consider here the MITC4 and MITC4+ shell elements which are very effective in the analysis of shells [5,6,7,8,9]. However, since the elements do not carry three rotational degrees of freedom at the nodes, they cannot directly be used in the modeling of intersection shells at large angles or shells with beam elements.

Another benefit of including the drill rotation in the formulations of shell elements is to possibly improve the element in-plane behavior. The possible improvement of the element behavior by using the drill rotation was first studied for plane-stress elements by Allman [10,11] and then, for example, also in Refs. [12,13,14,15]. The kinematics involved the inclusion of a quadratic interpolation of displacement at the fictitious mid-side nodes of the elements. However, the focus in these works was largely on using flat elements. An effective formulation for general shell elements is much more difficult to reach.

We should recall that considering the behavior of general shell structures, the membrane and bending actions are fully coupled and this coupling needs to be properly included *within the domain of each finite element* in the finite element model. Geometrically flat elements may not

properly represent this behavior and indeed not provide acceptable convergence behavior, see Ref. [1].

When developing a general shell element, difficulties can arise in passing the basic element tests, that is, the rigid body mode, isotropy and patch tests. Specifically, when considering the patch tests, only the minimum degrees of freedom to prevent a rigid body motion should be fixed, that is, the drill rotations should be left free [6,15], and this should be possible without special procedures, that is, without including artificial factors or stabilization schemes.

In this paper, we propose a new formulation to include the drill rotational degree of freedom for quadrilateral *continuum mechanics-based* shell elements (that, in general, are not of flat geometry). We apply the approach to our original MITC4 shell element [3,6] and the MITC4+ shell element [5,7]. We denote these elements by using the suffix “/D” to have the denotations “MITC4 / D” and “MITC4+ / D”. We study the element behaviors considering the basic tests including the patch tests in membrane, shear and bending actions, and their convergence behaviors in the analysis of shell structures, as proposed in Refs. [1–5]. These tests may also show an improved membrane behavior. In addition, we also illustrate the use of the novel elements in the solution of some nonlinear problems.

2. New shell finite elements

In this section, we briefly review the formulation of the MITC4 and

* Corresponding author.

E-mail address: Yeongbin.Ko@bentley.com (Y. Ko).

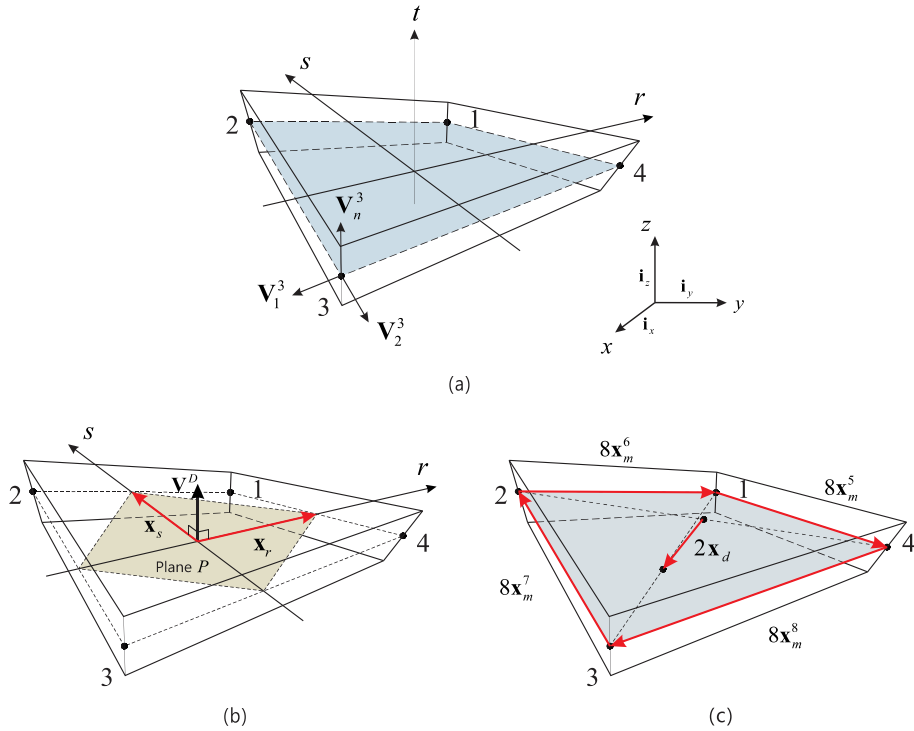


Fig. 1. A standard 4-node quadrilateral continuum mechanics-based shell finite element and geometry-vectors. (a) Element geometry. (b) Vectors related to the fictitious plane at the element center. (c) Vectors related to element distortions and edges.

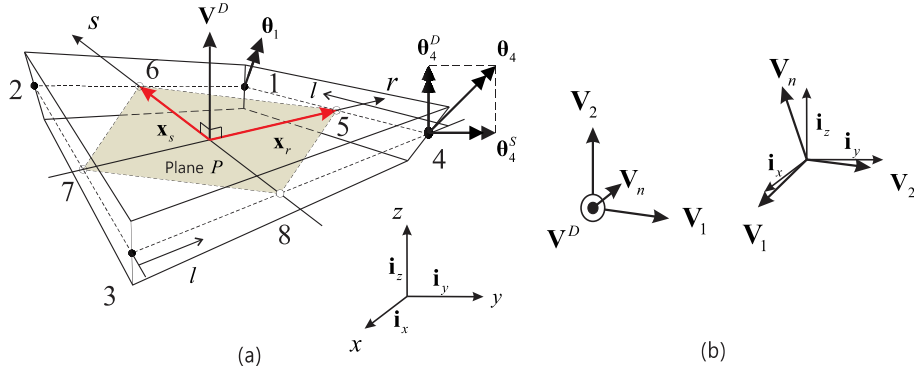


Fig. 2. Rotations and projections. (a) The drill rotation direction. (b) The coordinate systems for projecting rotations.

improved MITC4 + shell elements, and then enhance the element formulations by introducing the effects of the drilling rotations.

2.1. Geometry and displacement interpolations

The geometry of a standard 4-node continuum mechanics based quadrilateral shell finite element is interpolated using [4–8]

$$\mathbf{x}(r, s, t) = \sum_{i=1}^4 h_i(r, s) \mathbf{x}_i + \frac{t}{2} \sum_{i=1}^4 a_i h_i(r, s) \mathbf{V}_n^i \quad (1)$$

where $h_i(r, s)$ is the two-dimensional interpolation function of the standard isoparametric procedure corresponding to node i , \mathbf{x}_i is the position vector of node i in the global Cartesian coordinate system, and a_i and \mathbf{V}_n^i denote the shell thickness and the director vector at the node, respectively, see Fig. 1.

The isoparametric interpolation functions $h_i(r, s)$ are given by

$$h_i(r, s) = \frac{1}{4}(1 + \xi_i r)(1 + \eta_i s) \quad \text{with } i = 1, 2, 3, 4,$$

and

$$\begin{bmatrix} \xi_1 & \xi_2 & \xi_3 & \xi_4 \end{bmatrix} = \begin{bmatrix} 1 & -1 & -1 & 1 \end{bmatrix} \quad (2)$$

$$\begin{bmatrix} \eta_1 & \eta_2 & \eta_3 & \eta_4 \end{bmatrix} = \begin{bmatrix} 1 & 1 & -1 & -1 \end{bmatrix}$$

The corresponding displacement interpolation of the element is

$$\mathbf{u}(r, s, t) = \sum_{i=1}^4 h_i(r, s) \mathbf{u}_i + \frac{t}{2} \sum_{i=1}^4 a_i h_i(r, s) (\boldsymbol{\theta}_i \times \mathbf{V}_n^i) \quad (3a)$$

in which \mathbf{u}_i and $\boldsymbol{\theta}_i$ are the nodal displacement and rotation vectors in the global Cartesian coordinate system (i_x, i_y, i_z),

$$\mathbf{u}_i = u_x^i \mathbf{i}_x + u_y^i \mathbf{i}_y + u_z^i \mathbf{i}_z \quad (3b)$$

$$\boldsymbol{\theta}_i = \theta_x^i \mathbf{i}_x + \theta_y^i \mathbf{i}_y + \theta_z^i \mathbf{i}_z \quad (3c)$$

and \mathbf{V}_1^i and \mathbf{V}_2^i are unit vectors orthogonal to \mathbf{V}_n^i , which can be given by

$$\mathbf{V}_1^i = (\mathbf{i}_y \times \mathbf{V}_n^i) / \| \mathbf{i}_y \times \mathbf{V}_n^i \|; \quad \mathbf{V}_2^i = \mathbf{V}_n^i \times \mathbf{V}_1^i. \quad (3d)$$

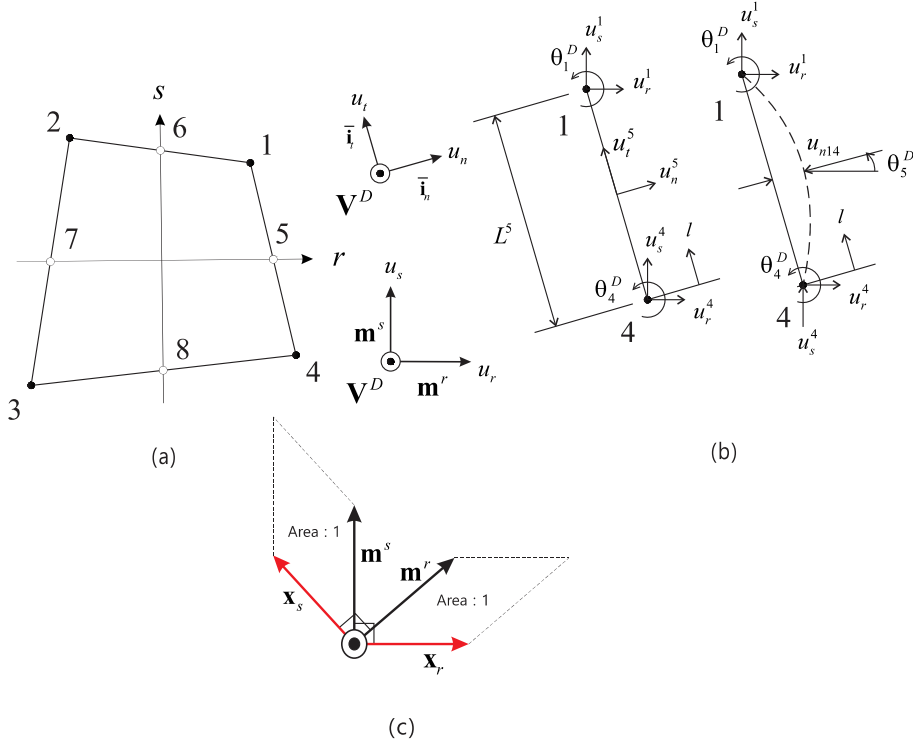


Fig. 3. Kinematics of in-plane rotations. (a) Locations of fictitious mid-side nodes. (b) Interpolation along the edges. (c) Directions of in-plane displacements.

We note that the geometry of the element \mathbf{x}_i is, in general, not a flat surface.

The geometry and displacement derivatives are given by

$$\mathbf{g}_i = \frac{\partial \mathbf{x}}{\partial r_i}, \mathbf{u}_i = \frac{\partial \mathbf{u}}{\partial r_i} \quad \text{with } r_1 = r, r_2 = s, r_3 = t. \quad (4a)$$

The covariant derivatives for the 4-node element can be further expressed as

$$\mathbf{g}_r = \frac{\partial \mathbf{x}}{\partial r} = \mathbf{x}_r + s\mathbf{x}_d, \mathbf{u}_r = \frac{\partial \mathbf{u}}{\partial r} = \mathbf{u}_r + s\mathbf{u}_d, \quad (4b)$$

$$\mathbf{g}_s = \frac{\partial \mathbf{x}}{\partial s} = \mathbf{x}_s + r\mathbf{x}_d, \mathbf{u}_s = \frac{\partial \mathbf{u}}{\partial s} = \mathbf{u}_s + r\mathbf{u}_d, \quad (4b)$$

with the following characteristic geometry and displacement vectors

$$\mathbf{x}_r = \frac{1}{4} \sum_{i=1}^4 \xi_i \mathbf{x}_i, \mathbf{x}_s = \frac{1}{4} \sum_{i=1}^4 \eta_i \mathbf{x}_i, \mathbf{x}_d = \frac{1}{4} \sum_{i=1}^4 \xi_i \eta_i \mathbf{x}_i, \quad (4c)$$

$$\mathbf{u}_r = \frac{1}{4} \sum_{i=1}^4 \xi_i \mathbf{u}_i, \mathbf{u}_s = \frac{1}{4} \sum_{i=1}^4 \eta_i \mathbf{u}_i, \mathbf{u}_d = \frac{1}{4} \sum_{i=1}^4 \xi_i \eta_i \mathbf{u}_i \quad (4c)$$

where the vectors \mathbf{x}_r , \mathbf{x}_s and \mathbf{x}_d shown in Fig. 1 arise naturally from the element geometry.

In order to pass the rigid body mode test, the drill rotation for a 4-node shell element needs to be defined from a single base. Considering the 4-node shell element, there is a plane P (see Fig. 1(b)) given by geometry derivative vectors that is always flat [7,8]. We define a normal vector to the plane at its center to establish the direction of the drill rotation, see \mathbf{V}^D (Fig. 2(a));

$$\mathbf{V}^D = \frac{\mathbf{x}_r \times \mathbf{x}_s}{\|\mathbf{x}_r \times \mathbf{x}_s\|}, \mathbf{x}_r = \mathbf{g}_r(0, 0, 0), \mathbf{x}_s = \mathbf{g}_s(0, 0, 0), \quad (5)$$

with \mathbf{g}_i in Eq. (4a).

In the formulation we distinguish between the rotation at the node

due to the action of the nodal drill (see Fig. 2(b)),

$$\theta_i^D = \theta_i^D \mathbf{V}^D \quad (6a)$$

and the standard rotation

$$\theta_i^S = \alpha_i \mathbf{V}_1^i + \beta_i \mathbf{V}_2^i \quad (6b)$$

where θ_i^D is the drill rotation about the direction of \mathbf{V}^D .

The total rotation at the node is the sum of the two rotations

$$\theta_i = \theta_i^S + \theta_i^D \quad (6c)$$

$$\theta_i = \alpha_i \mathbf{V}_1^i + \beta_i \mathbf{V}_2^i + \gamma_i \mathbf{V}_n^i \quad (6d)$$

and a change in the rotation γ_i is given by the change in θ_i^D

$$\delta\gamma_i = \delta\theta_i^D (\mathbf{V}_n^i \cdot \mathbf{V}^D) \quad (6e)$$

where as usual “ δ ” denotes “virtual”.

We also have that the total drill rotation is given by

$$\theta_i^D = \alpha_i (\mathbf{V}_1^i \cdot \mathbf{V}^D) + \beta_i (\mathbf{V}_2^i \cdot \mathbf{V}^D) + \gamma_i (\mathbf{V}_n^i \cdot \mathbf{V}^D) \quad (6f)$$

We note that the rotations $(\alpha_i, \beta_i, \gamma_i)$ in Eq. (6d) are only used to update the director vectors $(\mathbf{V}_1^i, \mathbf{V}_2^i, \mathbf{V}_n^i)$ [5,9], and the components in Eq. (6d) give directly the global components in Eq. (3c), and vice versa.

To establish the strain-displacement matrices of the element we apply Eqs. (6a) to (6c) sequentially. As we present below, we use the rotations θ_i^D in Eq. (6a) to establish the element strains due to the drilling rotations at the four corner nodes. Thereafter we add the strain components that are not due to the drilling rotations at the nodes.

The linear terms of the displacement-based covariant strain components are given by

$$e_{ij} = \frac{1}{2} (\mathbf{g}_i \cdot \mathbf{u}_j + \mathbf{g}_j \cdot \mathbf{u}_i) \quad (7)$$

We can write the covariant in-plane strain components in Eq. (7) as

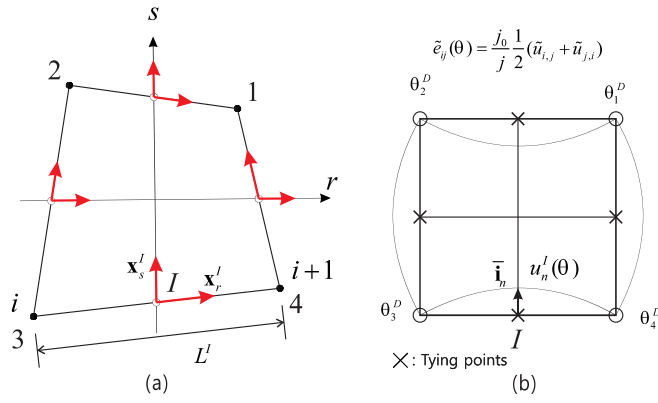


Fig. 4. Description of displacement tying. (a) The base vectors of each edge ($\mathbf{x}_r^I = \mathbf{g}_{r_i}|_{(r^I, s^I)}$) at the mid-point of the edge I). (b) Displacement field constructed from normal displacement due to drill rotation (deformation shown with $\theta_1^D = 0$, $\theta_2^D = -\theta$, $\theta_3^D = \theta$, $\theta_4^D = -\theta$).

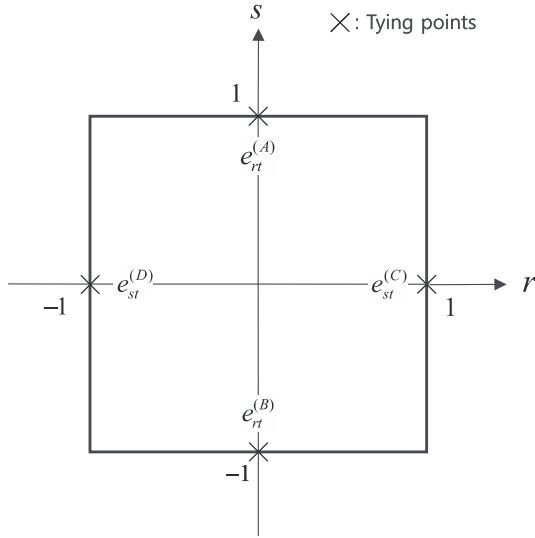


Fig. 5. Tying positions (A), (B), (C) and (D) for the assumed transverse shear strain field of the MITC4 shell element. The constant transverse shear strain conditions are imposed along the edges.

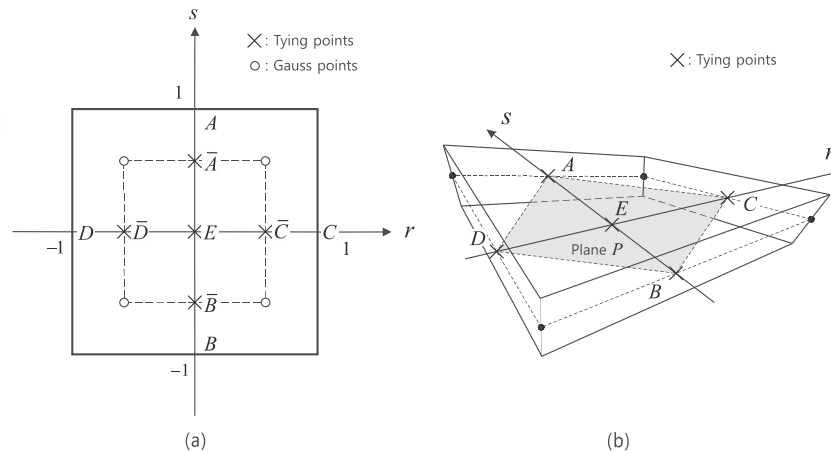


Fig. 6. Tying positions for the assumed membrane shear strain field for the MITC4 + shell elements. (a) For the internally embedded strain \bar{e}_{ij}^m . (b) For the final shell membrane strain e_{ij}^m .

$$\bar{e}_{ij} = \bar{e}_{ij}^m + t \bar{e}_{ij}^{b1} + t^2 \bar{e}_{ij}^{b2} \text{ with } i, j = 1, 2 \quad (8a)$$

$$\bar{e}_{ij}^m = \frac{1}{2} \left(\frac{\partial \mathbf{x}_m}{\partial r_i} \cdot \frac{\partial \mathbf{u}_m}{\partial r_j} + \frac{\partial \mathbf{x}_m}{\partial r_j} \cdot \frac{\partial \mathbf{u}_m}{\partial r_i} \right) \quad (8b)$$

$$\bar{e}_{ij}^{b1} = \frac{1}{2} \left(\frac{\partial \mathbf{x}_m}{\partial r_i} \cdot \frac{\partial \mathbf{u}_b}{\partial r_j} + \frac{\partial \mathbf{x}_m}{\partial r_j} \cdot \frac{\partial \mathbf{u}_b}{\partial r_i} + \frac{\partial \mathbf{x}_b}{\partial r_i} \cdot \frac{\partial \mathbf{u}_m}{\partial r_j} + \frac{\partial \mathbf{x}_b}{\partial r_j} \cdot \frac{\partial \mathbf{u}_m}{\partial r_i} \right) \quad (8c)$$

$$\bar{e}_{ij}^{b2} = \frac{1}{2} \left(\frac{\partial \mathbf{x}_b}{\partial r_i} \cdot \frac{\partial \mathbf{u}_b}{\partial r_j} + \frac{\partial \mathbf{x}_b}{\partial r_j} \cdot \frac{\partial \mathbf{u}_b}{\partial r_i} \right) \quad (8d)$$

with

$$\mathbf{x}_m = \sum_{i=1}^4 h_i(r, s) \mathbf{x}_i, \mathbf{x}_b = \frac{1}{2} \sum_{i=1}^4 a_i h_i(r, s) \mathbf{V}_n^i, \quad (9a)$$

$$\mathbf{u}_m = \sum_{i=1}^4 h_i(r, s) \mathbf{u}_i, \mathbf{u}_b = \frac{1}{2} \sum_{i=1}^4 a_i h_i(r, s) (\boldsymbol{\theta}_i \times \mathbf{V}_n^i) \quad (9b)$$

The first term \bar{e}_{ij}^m in Eq. (8a) is the covariant in-plane membrane strain at the shell mid-surface ($t = 0$), and the remaining terms are the covariant in-plane strains due to bending.

2.2. New interpolation functions and development of kinematics

In the formulation to include the drill rotation we create just a single additional interpolation function (along the edges) to have stability of the element for in-plane rotations, pass the patch test when the rotation is free (without use of a special procedures, see Refs. [5,6,7,15]) and improve the element behavior.

Hence, consider in addition to the interpolation functions $h_i(r, s)$ corresponding to the corner nodes, see Eq. (2), also the mid-side node interpolation functions corresponding to the “fictitious” nodes 5, 6, 7, 8 located at the mid-points of the element sides as shown in Fig. 3(a)

$$\begin{aligned} & [h_5 \ h_6 \ h_7 \ h_8] \\ & = \left[\frac{1}{2}(1-s^2)(1+r) \ \frac{1}{2}(1-r^2)(1+s) \ \frac{1}{2}(1-s^2)(1-r) \ \frac{1}{2}(1-r^2)(1-s) \right] \end{aligned} \quad (10)$$

where we shall use the following notation with I denoting the edge and m the fictitious mid-side node $h_{m,r}^I = h_{l,r}$, $h_{m,s}^I = h_{l,s}$. To proceed we then simplify the derivatives of these functions and use

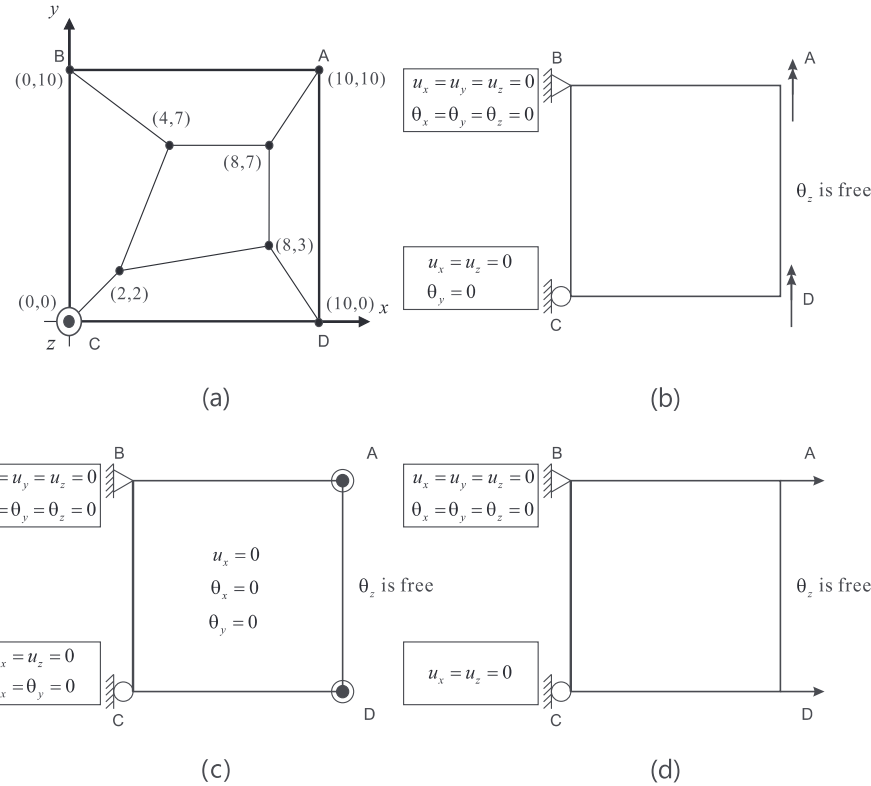


Fig. 7. Patch tests. (a) Mesh used. (b) Bending patch test. (c) Shearing patch test. (d) Extension patch test.

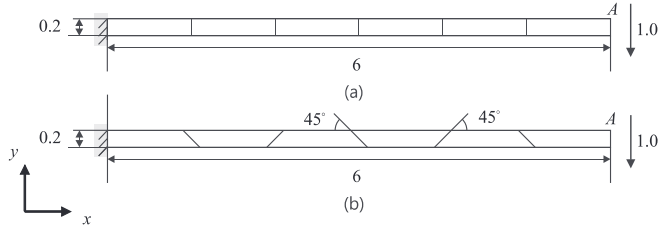


Fig. 8. Straight slender cantilever ($E = 1.0 \times 10^7$, thickness 0.1, $\nu = 0.3$). (a) Mesh type 1, (b) Mesh type 2.

Table 1

Vertical deflection ($-u_y$) at the tip (average of displacements at nodes near point A) for the slender cantilever problems.

Elements	Mesh	
	Mesh type 1	Mesh type 2
MITC4	0.010088	0.00290874
MITC4-IC	0.107328	0.00569730
MITC4 / D	0.0976755	0.00550604
MITC4+ / D	0.0976755	0.00550838
Reference solution	0.1081	

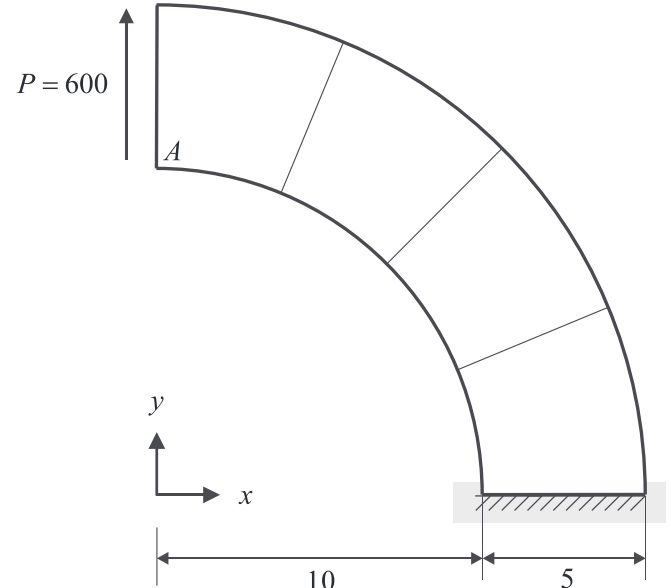


Fig. 9. Thick curved beam problem (Plane stress condition, 1 \times 4 mesh, $E = 1.0 \times 10^3$ and $\nu = 0.0$, unit thickness).

Table 2

Vertical displacements at the tip (point A) for the curved beam problem.

Elements	Regular mesh		
	1 × 2	1 × 4	1 × 8
MITC4	22.5988	57.9325	79.9218
MITC4-IC	52.2291	84.6070	89.3023
MITC4 / D	51.2489	84.1086	89.1698
MITC4+ / D	51.2692	84.1444	89.2077
Reference solution	90.1		

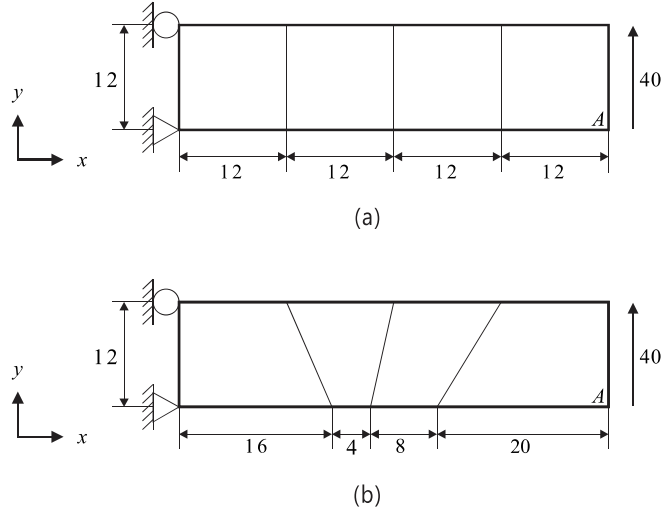


Fig. 10. Cantilever beam with roller support (Plane stress condition, 1×4 mesh, $E = 3.0 \times 10^4$ and $\nu = 0.0$, unit thickness). (a) Regular mesh. (b) Distorted mesh.

Table 3

Vertical displacements at the tip (point A) for the cantilever problem.

Elements	Regular mesh	Distorted mesh
MITC4	0.235608	0.203966
MITC4-IC	0.347810	0.342552
MITC4 / D	0.347810	0.339249
MITC4+ / D	0.347810	0.341015
Reference solution	0.347810	

$$\begin{bmatrix} \tilde{h}_{5,r} & \tilde{h}_{6,r} & \tilde{h}_{7,r} & \tilde{h}_{8,r} \end{bmatrix} = \begin{bmatrix} 0 & \frac{1}{2}(-2r)(1+s) & 0 & \frac{1}{2}(-2r)(1-s) \end{bmatrix},$$

$$\tilde{h}_{m,r}^I = \tilde{h}_{I,r}, \quad (11a)$$

$$\begin{bmatrix} \tilde{h}_{5,s} & \tilde{h}_{6,s} & \tilde{h}_{7,s} & \tilde{h}_{8,s} \end{bmatrix} = \begin{bmatrix} \frac{1}{2}(-2s)(1+r) & 0 & \frac{1}{2}(-2s)(1-r) & 0 \end{bmatrix},$$

$$\tilde{h}_{m,s}^I = \tilde{h}_{I,s} \quad (11b)$$

where we use the “curl” to signify that simplified functions are used. Here the zeros in Eq. (11b) are introduced to avoid a higher order of numerical integration than used with the original elements. The important point is that this simplification can be used with the basic and patch tests still satisfied, and we also see good convergence behavior.

We remark that the idea of using modified higher-order interpolation functions can be also found in Refs. [16,17].

Next, we need an expression for the displacements at the fictitious nodes, and we employ the expressions proposed by Allman [10,11] and Cook [18]. We use for the tangential displacement identified using the

subscript t along the edge at node 5, see Fig. 3(b),

$$u_t^5(l) = \left(1 - \frac{l}{L_5}\right) u_n^4 + \frac{l}{L_5} u_t^1 \quad (12a)$$

where the superscripts 1, 4, 5 denote the nodal values, the length of edge is L_5 and l is the coordinate value along the edge, see Fig. 2(a) and Fig. 3(b). The normal displacement along the edge of node 5 is given by a quadratic interpolation

$$u_n^5(l) = \left(1 - \frac{l}{L_5}\right) u_n^4 + \frac{l}{L_5} u_n^1 + \frac{4l}{L_5} \left(1 - \frac{l}{L_5}\right) \theta_n^5 \quad (12b)$$

where the last term corresponds to the normal displacement at node 5 (along the edge of node 5 between nodes 1 and 4) measured from the linear displacement given by the first two terms on the right-hand side of Eq. (12b).

The value of θ_n^5 is measured as all other nodal rotations, see discussion below, and can be obtained from the boundary condition

$$\frac{\partial u_n^5}{\partial l} \Big|_{l=L_5} - \frac{\partial u_n^5}{\partial l} \Big|_{l=0} = -\theta_4 + \theta_1 \quad (12c)$$

Hence

$$\theta_n^5 = \frac{L_5}{8} (\theta_4 - \theta_1) = \frac{L_5}{8} (\theta_4^D - \theta_1^D) \quad (12d)$$

We use the same assumptions for the displacements due to drill rotations along the other 3 edges on which the mid-side fictitious nodes 6, 7 and 8 are located.

A key point in our solution procedure is that we utilize the vector \mathbf{V}^D at the element center about which to measure all rotations at the nodal points (that is, we use $\theta_i = \theta_i^D$ for all nodes $i = 1, 2, \dots, 8$, hence all nodal drill rotations are measured as drill rotations about the same vector \mathbf{V}^D). It then follows that continuity between edge displacements is always obtained, and the rigid body mode test is always satisfied even when the shell element is curved.

Our objective is to now obtain the total element strain over the element domain.

Consider the displacements corresponding to the in-plane directions shown in Fig. 3(c). The transformation to tangential and normal directions in Fig. 3(b) gives

$$u_r^I \mathbf{m}^r + u_s^I \mathbf{m}^s = u_n^I \bar{\mathbf{i}}_n + u_t^I \bar{\mathbf{i}}_t \quad (13a)$$

in which $\mathbf{x}_{r_i} \cdot \mathbf{m}^r = \delta_{ij}$ where δ_{ij} is the Kronecker delta.

The tangential and normal directions at the edge I are

$$\bar{\mathbf{i}}_t = \mathbf{x}_m^I / \| \mathbf{x}_m^I \|, \quad \bar{\mathbf{i}}_n = \bar{\mathbf{i}}_t \times \mathbf{V}^D \quad (13b)$$

and we have

$$[\mathbf{x}_m^5 \ \mathbf{x}_m^6 \ \mathbf{x}_m^7 \ \mathbf{x}_m^8] = \left[\frac{1}{8}(\mathbf{x}_4 - \mathbf{x}_1) \ \frac{1}{8}(\mathbf{x}_1 - \mathbf{x}_2) \ \frac{1}{8}(\mathbf{x}_2 - \mathbf{x}_3) \ \frac{1}{8}(\mathbf{x}_3 - \mathbf{x}_4) \right] \quad (13c)$$

The displacement field introduced in Eq. (13a) will lead to a strain definition in covariant coordinates. Note that unlike the displacements which occur in the element natural directions (r and s), the displacements in Eq. (13a) are defined using the fixed coordinate system (\mathbf{m}^r and \mathbf{m}^s), hence, additional terms due to a change in the basis vectors (\mathbf{x}_r and \mathbf{x}_s) will not arise. The coordinate systems defined at each edge (\mathbf{x}_r^I and \mathbf{x}_s^I) are shown in Fig. 4(a). Here $\mathbf{x}_r^I = \mathbf{g}_{r_i}|_{(r^I, s^I)}$ at the mid-point of the edge I .

From Eq. (13a) we obtain for the displacement components on the edges

$$u_r^I = u_n^I \bar{\mathbf{i}}_n \cdot \mathbf{x}_r^I + u_t^I \bar{\mathbf{i}}_t \cdot \mathbf{x}_r^I, \quad u_s^I = u_n^I \bar{\mathbf{i}}_n \cdot \mathbf{x}_s^I + u_t^I \bar{\mathbf{i}}_t \cdot \mathbf{x}_s^I. \quad (14a)$$

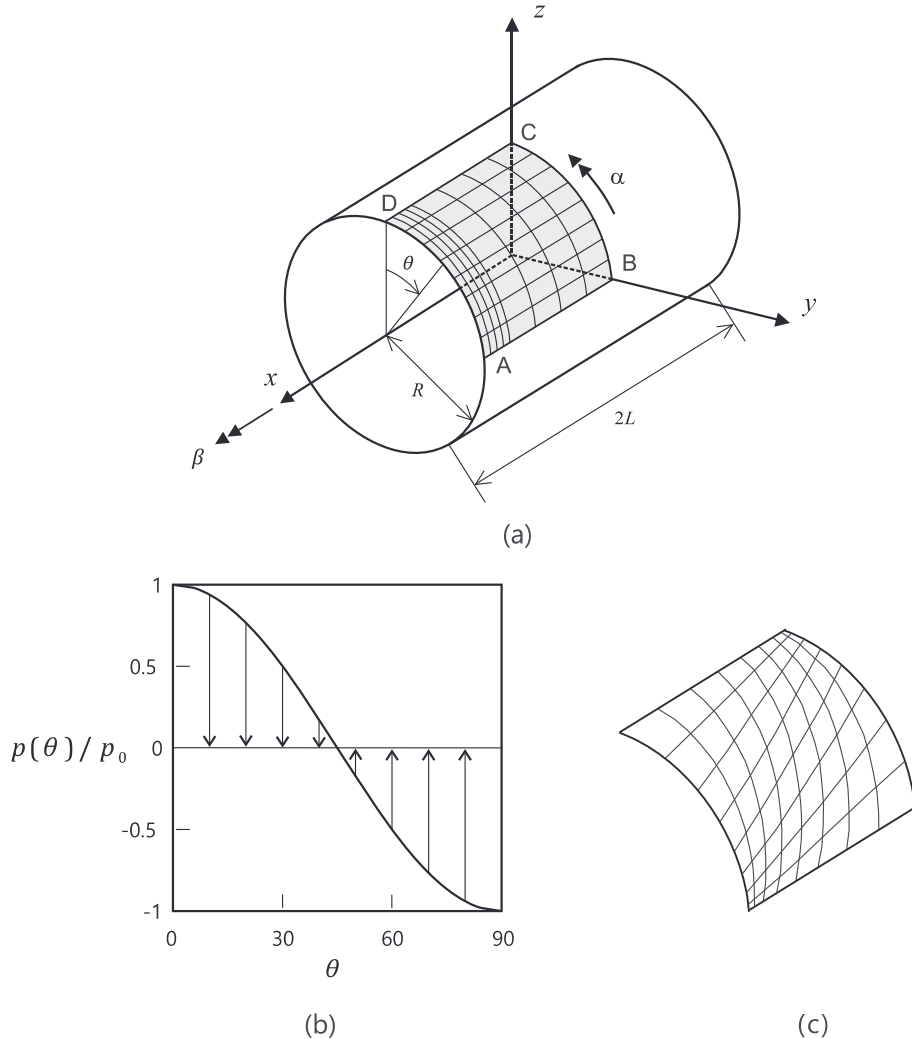


Fig. 11. Cylindrical shell problem ($E = 2.0 \times 10^{11}$, $\nu = 1/3$, $L = 1.0$ and $p_0 = 1.0$). (a) Problem description with graded regular mesh (8 \times 8 mesh, $t/L = 1/1000$). (b) Pressure distribution. (c) Distorted mesh used (8 \times 8 mesh).

the element to pass the patch test, we use

$$u_r^I = u_\theta^I(l) \bar{\mathbf{i}}_n \cdot \mathbf{x}_r^I, \quad u_s^I = u_\theta^I(l) \bar{\mathbf{i}}_n \cdot \mathbf{x}_s^I, \quad (14b)$$

where $u_\theta^I(l)$ is the drill rotational effect along the side I and at the point given by l , for example,

$$u_\theta^5(l) = \frac{4l}{L_5} \left(1 - \frac{l}{L_5} \right) \theta_n^5, \text{ similar for edges 6, 7, 8.} \quad (14c)$$

Here u_θ^5 is the displacement normal to the edge due to the drill rotation at the edge (given by the drill rotations at nodes 1 and 4).

Using the above equations, we have for each edge I

$$u_r^I(l) = \frac{1}{\|\mathbf{x}_m^I\|} (u_\theta^I(l) \mathbf{x}_m^I \times \mathbf{V}^D \cdot \mathbf{x}_r^I) \quad (14d)$$

$$u_s^I(l) = \frac{1}{\|\mathbf{x}_m^I\|} (u_\theta^I(l) \mathbf{x}_m^I \times \mathbf{V}^D \cdot \mathbf{x}_s^I) \quad (14e)$$

The continuous displacements over the elements due to the drill rotations are then obtained by interpolation and summing over the respective edges I

$$u_r = h_m^I u_r^I \left(\frac{L_I}{2} \right) = \frac{1}{\|\mathbf{x}_m^I\|} \left[-h_m^I u_\theta^I \left(\frac{L_I}{2} \right) \mathbf{x}_r^I \times \mathbf{V}^D \right] \cdot \mathbf{x}_m^I \quad (15a)$$

$$u_s = h_m^I u_s^I \left(\frac{L_I}{2} \right) = \frac{1}{\|\mathbf{x}_m^I\|} \left[-h_m^I u_\theta^I \left(\frac{L_I}{2} \right) \mathbf{x}_s^I \times \mathbf{V}^D \right] \cdot \mathbf{x}_m^I \quad (15b)$$

in which we use $l = \frac{L_I}{2}$ for each edge because the tying is performed at the fictitious nodes and also $\|\mathbf{x}_m^I\| = \frac{L_I}{8}$.

Using the geometric relations (Eq. (12d) and (13c)), the displacement fields assumed in Eq. (15) reduce to

$$\begin{aligned} \bar{u}_r(\theta) &= h_l (\theta_{i+1}^D - \theta_i^D) \mathbf{x}_m^I \cdot (-\mathbf{x}_r^I \times \mathbf{V}^D) \\ \bar{u}_s(\theta) &= -h_l (\theta_{i+1}^D - \theta_i^D) \mathbf{x}_m^I \cdot (\mathbf{x}_s^I \times \mathbf{V}^D) \end{aligned} \quad (16a)$$

where the edge I corresponds to nodes i and $i + 1$. Eq. (16a) is the displacement-based interpolation of the drill effect with the standard mid-side interpolation $h_m^I = h_l$ given in Eq. (10).

Next we use the ‘assumed interpolation’ at the edges. By applying Eq. (11) to Eq. (16a), we obtain

$$\begin{aligned} \tilde{u}_r(\theta) &= \tilde{h}_m^I (\theta_{i+1}^D - \theta_i^D) \mathbf{x}_m^I \cdot (-\mathbf{x}_r^I \times \mathbf{V}^D), \\ \tilde{u}_s(\theta) &= -\tilde{h}_m^I (\theta_{i+1}^D - \theta_i^D) \mathbf{x}_m^I \cdot (\mathbf{x}_s^I \times \mathbf{V}^D) \end{aligned} \quad (16b)$$

As we mentioned earlier, all drill-rotations are defined for the curved shell as rotations about the normal \mathbf{V}^D to the plane P formed by adjoining the fictitious nodes. The calculated values are then projected

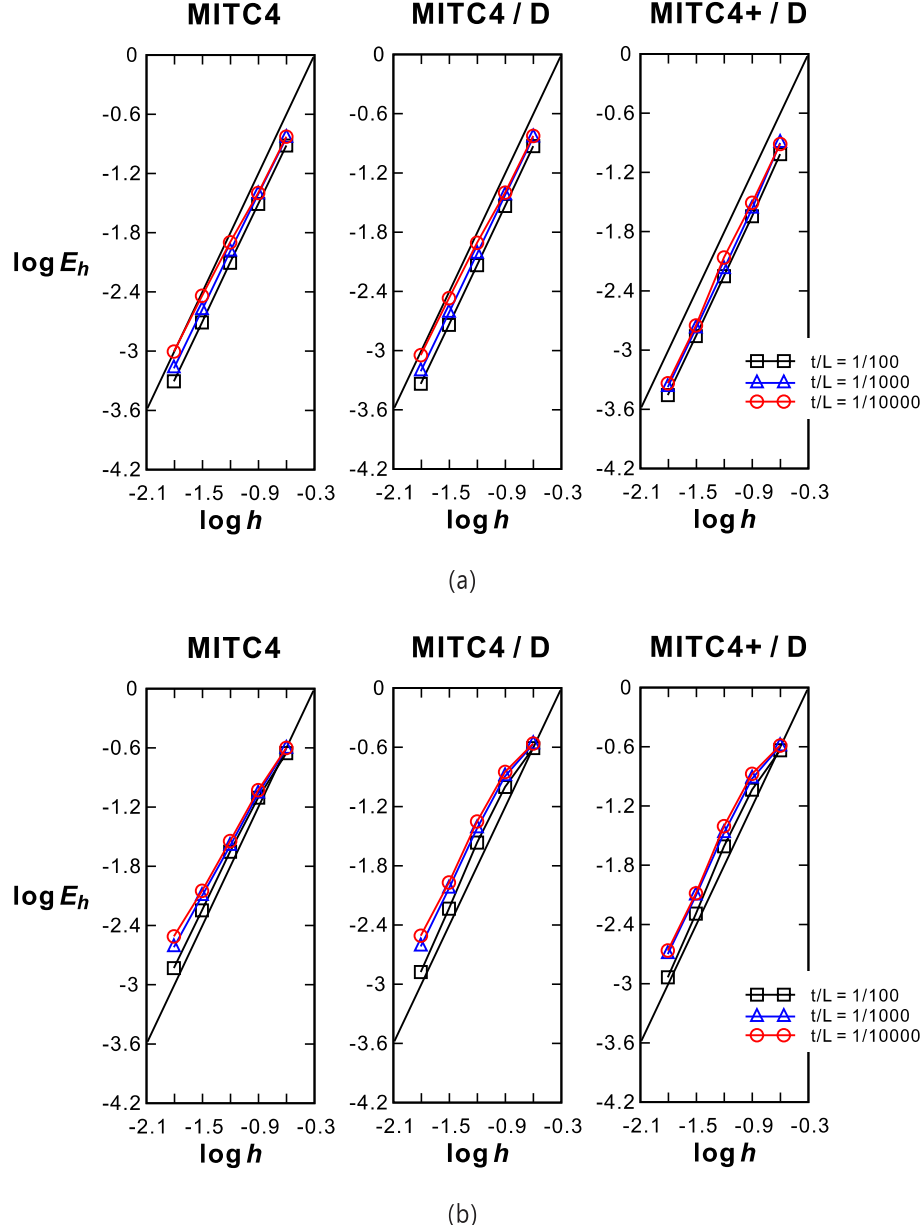


Fig. 12. Convergence curves for the clamped cylindrical shell problem with (a) the graded regular and (b) distorted meshes. The bold line represents the optimal convergence rate.

back to the nodal locations using Eq. (6). Proceeding this way, that is, using the rotations about \mathbf{V}^D , leads to satisfying the element isotropy test and rigid body modes test, and even when the element is not flat (Fig. 1(c) and 2(b)).

In addition, it is valuable to note that using the single normal to the plane P results in an overall improved element behavior when compared to using a changing normal over the element geometry.

2.3. The new membrane strain due to the drilling degrees of freedom

Using the displacements in Eqs. (15) to (16), we have the strain as

$$\bar{e}_{ij}(\theta) = \frac{1}{2} (\bar{u}_{ij} + \bar{u}_{ji}) \quad (17a)$$

$$\tilde{e}_{ij}(\theta) = \frac{j_0}{j} \frac{1}{2} (\tilde{u}_{ij} + \tilde{u}_{ji}) \quad (17b)$$

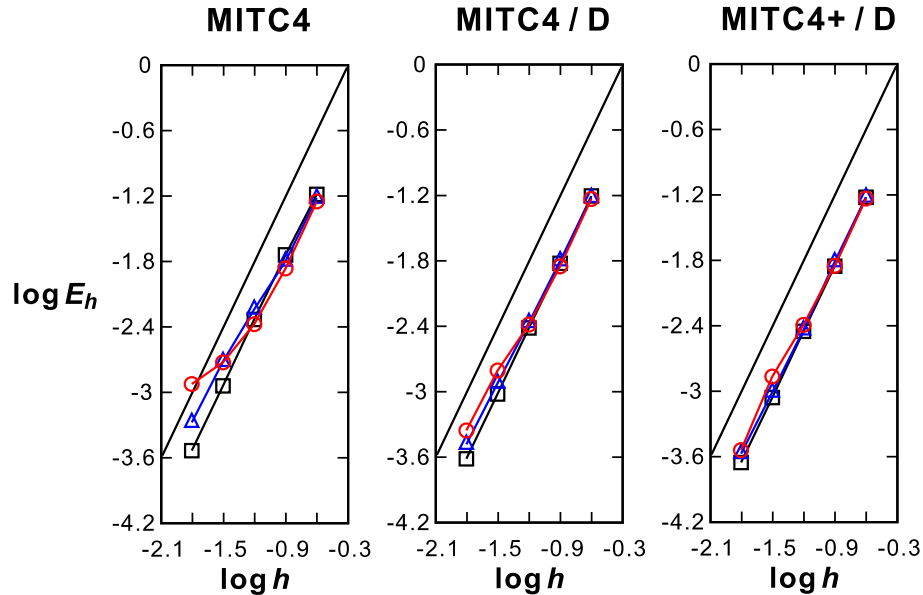
with the indices i and $j = 1, 2$ corresponding to $r_1 = r$ and $r_2 = s$. We also use $j = \det[\mathbf{g}_r \ \mathbf{g}_s \ \mathbf{g}_t]|_{(r,s,0)}$ and $j_0 = j(0,0,0)$. The strain in Eq. (17a) is the usual displacement-based strain and the strain in Eq. (17b) is an approximation that is simple, relative to the value used in Ref. [20], and when used leads to satisfying the patch tests.

Substituting from Eq. (16b) into Eq. (17b), the individual components for the “drill-membrane” strain (identified using the superscript ‘md’) are

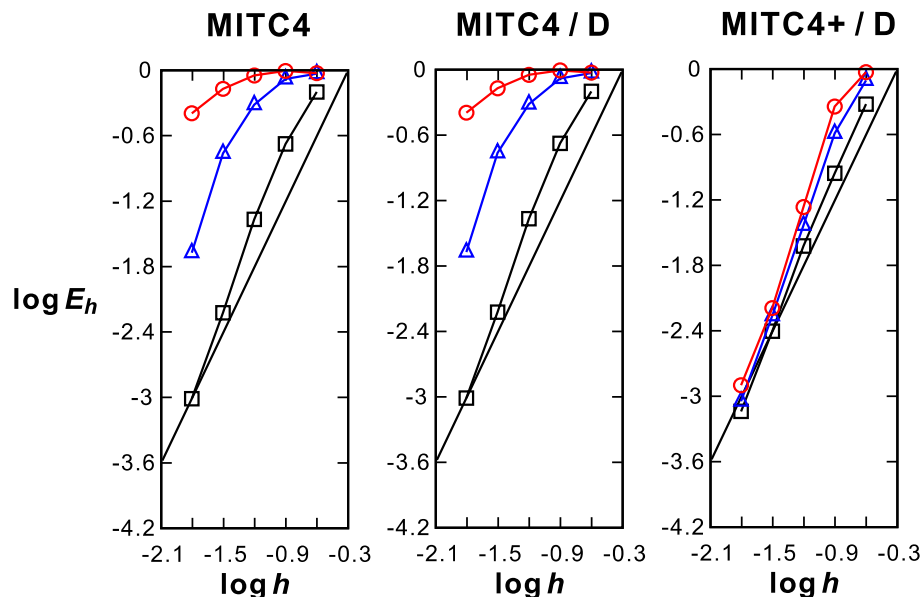
$$\tilde{e}_{rr}^{md} = (j_0/j) \tilde{u}_{r,r}(\theta) = (j_0/j) \tilde{h}_{m,r}^I(\theta_{i+1}^D - \theta_i^D) \mathbf{x}_m^I \cdot (-\mathbf{x}_r^I \times \mathbf{V}^D)$$

$$\tilde{e}_{ss}^{md} = (j_0/j) \tilde{u}_{s,s}(\theta) = -(j_0/j) \tilde{h}_{m,s}^I(\theta_{i+1}^D - \theta_i^D) \mathbf{x}_m^I \cdot (\mathbf{x}_s^I \times \mathbf{V}^D)$$

$$\begin{aligned} \tilde{e}_{rs}^{md} &= (1/2)(j_0/j) (\tilde{u}_{s,r}(\theta) + \tilde{u}_{r,s}(\theta)) \\ &= (1/2)(j_0/j) [\tilde{h}_{m,s}^I \mathbf{x}_m^I \cdot (-\mathbf{x}_r^I \times \mathbf{V}^D) - \tilde{h}_{m,r}^I \mathbf{x}_m^I \cdot (\mathbf{x}_s^I \times \mathbf{V}^D)] (\theta_{i+1}^D - \theta_i^D) \end{aligned} \quad (18)$$



(a)



(b)

Fig. 13. Convergence curves for the free cylindrical shell problem with (a) the graded regular and (b) distorted meshes. The bold line represents the optimal convergence rate.

We note that these expressions are given using the individual nodal drill rotations θ_i^D and that these expressions need to be summed over the edges I connecting nodes i and $i + 1$.

Hence the assumed strain–displacement relations corresponding to the nodal drill rotations are

$$\begin{bmatrix} \tilde{\epsilon}_{rr}^{md} \\ \tilde{\epsilon}_{ss}^{md} \\ \tilde{\epsilon}_{rs}^{md} \end{bmatrix} = \tilde{\mathbf{B}} \begin{bmatrix} \theta_1^D \\ \theta_2^D \\ \theta_3^D \\ \theta_4^D \end{bmatrix}, \tilde{\mathbf{B}} = \frac{j_0}{j} \begin{bmatrix} \tilde{\mathbf{B}}_{rr} \\ \tilde{\mathbf{B}}_{ss} \\ \tilde{\mathbf{B}}_{rs} \end{bmatrix} \quad (19a)$$

$$\begin{aligned} \tilde{\mathbf{B}}_{rr} &= \left[\tilde{h}_{m,r}^5 c_r^5 - \tilde{h}_{m,r}^6 c_r^6 \quad \tilde{h}_{m,r}^6 c_r^6 - \tilde{h}_{m,r}^7 c_r^7 \quad \tilde{h}_{m,r}^7 c_r^7 - \tilde{h}_{m,r}^8 c_r^8 \quad \tilde{h}_{m,r}^8 c_r^8 - \tilde{h}_{m,r}^5 c_r^5 \right] \\ \tilde{\mathbf{B}}_{ss} &= \left[-\tilde{h}_{m,s}^5 c_s^5 + \tilde{h}_{m,s}^6 c_s^6 \quad -\tilde{h}_{m,s}^6 c_s^6 + \tilde{h}_{m,s}^7 c_s^7 \quad -\tilde{h}_{m,s}^7 c_s^7 + \tilde{h}_{m,s}^8 c_s^8 \quad -\tilde{h}_{m,s}^8 c_s^8 + \tilde{h}_{m,s}^5 c_s^5 \right] \\ \tilde{\mathbf{B}}_{rs} &= \frac{1}{2} \left(\left[-\tilde{h}_{m,r}^5 c_s^5 + \tilde{h}_{m,r}^6 c_s^6 \quad -\tilde{h}_{m,r}^6 c_s^6 + \tilde{h}_{m,r}^7 c_s^7 \quad -\tilde{h}_{m,r}^7 c_s^7 + \tilde{h}_{m,r}^8 c_s^8 \quad -\tilde{h}_{m,r}^8 c_s^8 + \tilde{h}_{m,r}^5 c_s^5 \right] \right. \\ &\quad \left. + \left[\tilde{h}_{m,s}^5 c_r^5 - \tilde{h}_{m,s}^6 c_r^6 \quad \tilde{h}_{m,s}^6 c_r^6 - \tilde{h}_{m,s}^7 c_r^7 \quad \tilde{h}_{m,s}^7 c_r^7 - \tilde{h}_{m,s}^8 c_r^8 \quad \tilde{h}_{m,s}^8 c_r^8 - \tilde{h}_{m,s}^5 c_r^5 \right] \right), \end{aligned} \quad (19b)$$

$$c_r^I = \mathbf{x}_m^I \cdot (-\mathbf{x}_r^I \times \mathbf{V}^D), c_s^I = \mathbf{x}_m^I \cdot (\mathbf{x}_s^I \times \mathbf{V}^D) \quad (19c)$$

with the membrane coefficients c_r^I and c_s^I per edge I . These expressions can also be written as in simpler form

$$\begin{aligned} \tilde{\mathbf{B}}_{rr} &= \left[-\tilde{h}_{m,r}^6 c_r^6 \quad \tilde{h}_{m,r}^6 c_r^6 \quad -\tilde{h}_{m,r}^8 c_r^8 \quad \tilde{h}_{m,r}^8 c_r^8 \right] \\ \tilde{\mathbf{B}}_{ss} &= \left[-\tilde{h}_{m,s}^5 c_s^5 \quad \tilde{h}_{m,s}^7 c_s^7 \quad -\tilde{h}_{m,s}^7 c_s^7 \quad \tilde{h}_{m,s}^5 c_s^5 \right] \\ \tilde{\mathbf{B}}_{rs} &= (1/2) \left(\left[\tilde{h}_{m,r}^6 c_s^6 \quad -\tilde{h}_{m,r}^6 c_s^6 \quad \tilde{h}_{m,r}^8 c_s^8 \quad -\tilde{h}_{m,r}^8 c_s^8 \right] \right. \\ &\quad \left. + \left[\tilde{h}_{m,s}^5 c_r^5 \quad -\tilde{h}_{m,s}^7 c_r^7 \quad \tilde{h}_{m,s}^7 c_r^7 \quad -\tilde{h}_{m,s}^5 c_r^5 \right] \right) \end{aligned} \quad (19d)$$

Here we used the derivatives in Eq. (11) and edge coefficients c_r^I and c_s^I ($I = 5, 6, 7, 8$).

Eqs. (18) and (19d) give the strain field used in the present study, attained from the displacements with the assumed interpolations in Eq. (11), expressed in a simple explicit form. The equations are useful for the implementation of the element.

However, in addition, we can also establish a physical meaning of the strain field, using the MITC technique, and this meaning establishes also the edge coefficients used in Eq. (19). We present this derivation in Appendix A.

2.4. The transverse shear and in-plane strains

Considering the element transverse shear strain, for the MITC4 and MITC4 + shell elements the strain field is based on the now classical assumption a constant covariant transverse shear strain conditions along the edges [6,19],

$$\tilde{e}_{rt} = \frac{1}{2}(1+s)e_{rt}^{(A)} + \frac{1}{2}(1-s)e_{rt}^{(B)}, \tilde{e}_{st} = \frac{1}{2}(1+r)e_{st}^{(C)} + \frac{1}{2}(1-r)e_{st}^{(D)} \quad (20)$$

where the tying points are shown in Fig. 5, and transverse shear strains are obtained from Eq. (7).

Considering the element in-plane strain, the final drill-membrane strain is obtained by a transformation of Eq. (18) to the element natural coordinate system (the (r, s) system)

$$e_{ij}^{md} = (\mathbf{g}_i \cdot \mathbf{g}^k)(\mathbf{g}_j \cdot \mathbf{g}^l) \tilde{e}_{kl}^{md} \quad (21)$$

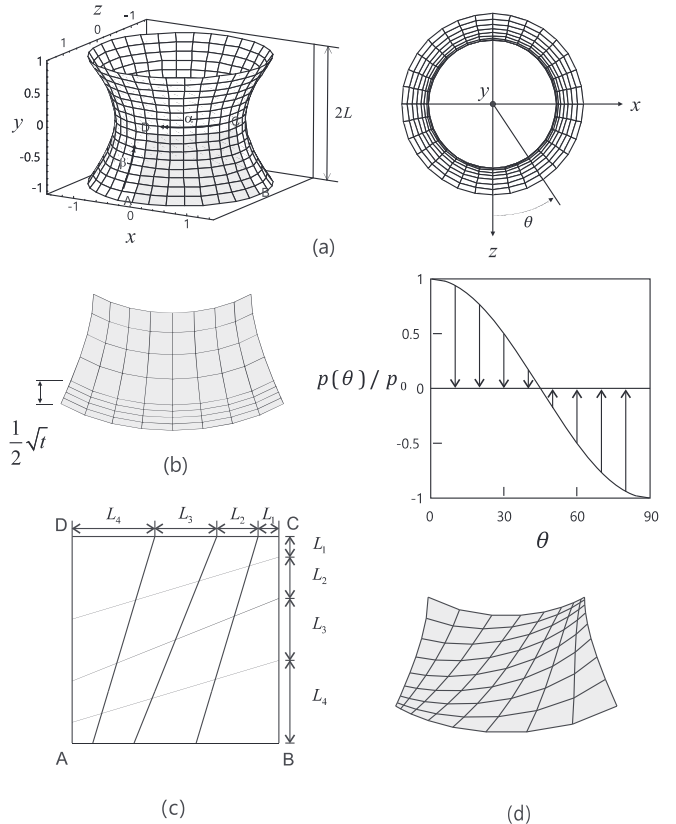


Fig. 14. Hyperboloid shell problem ($E = 2.0 \times 10^{11}$, $\nu = 1/3$, $L = 1.0$ and $p_0 = 1.0$). (a) Problem description. (b) Graded regular mesh (8×8 mesh, $t/L = 1/1000$). (c) Distorted mesh pattern (4×4 mesh). (d) Distorted mesh used (8×8 mesh).

with $\bar{\mathbf{g}}_i \cdot \bar{\mathbf{g}}^k = \delta_{ik}$, $\bar{\mathbf{g}}_i = \mathbf{g}_i(0, 0, 0) = \mathbf{x}_{ri}$ and $\bar{\mathbf{g}}^i = \mathbf{g}^i(0, 0, 0) = \mathbf{m}^ri$. Hence the base vectors $\bar{\mathbf{g}}_i$ and $\bar{\mathbf{g}}^i$ are constant over the element domain. Note that for the MITC shell elements, the strain in Eq. (21) is calculated only once through the thickness t , and the calculation of the coefficients c_r^I , c_s^I and $(\mathbf{g}_i \cdot \bar{\mathbf{g}}^k)$ is only performed once per each element.

Considering next the individual elements, when including the drill-membrane strain into the standard MITC4 element, the in-plane strain in Eq. (9a) is modified to be.

$$e_{ij} = e_{ij}^m + e_{ij}^{md} + t e_{ij}^{b1} + t^2 e_{ij}^{b2} \quad \text{with } i, j = 1, 2 \quad (22a)$$

This element is denoted as ‘MITC4 / D’. We also have for this element

$$e_{ij}^m(r, s) = (\mathbf{g}_i \cdot \bar{\mathbf{g}}^k)(\mathbf{g}_j \cdot \bar{\mathbf{g}}^l) \Big|_{(r, s, 0)} \bar{e}_{kl}^m \quad (22b)$$

$$\bar{e}_{ij}^m(r, s) = (\bar{\mathbf{g}}_i \cdot \mathbf{g}^k)(\bar{\mathbf{g}}_j \cdot \mathbf{g}^l) \Big|_{(r, s, 0)} e_{kl}^m = \bar{g}_i^k g_j^l e_{kl}^m \quad (22c)$$

with $\bar{g}_i^j = (\bar{\mathbf{g}}_i \cdot \mathbf{g}^j) \Big|_{(r, s, 0)}$.

Here, \bar{e}_{ij}^m is the “standard” displacement-based strain but defined using the element center coordinate to establish $(\bar{\mathbf{g}}_i)$. Further, the standard membrane strain e_{ij}^m can be expanded as

$$e_{rr}^m = e_{rr}|_{con.} + e_{rr}|_{lin.} \cdot s + e_{rs}|_{bil.} \cdot s^2$$

$$e_{ss}^m = e_{ss}|_{con.} + e_{ss}|_{lin.} \cdot r + e_{rs}|_{bil.} \cdot r^2$$

$$e_{rs}^m = e_{rs}|_{con.} + \frac{1}{2} e_{rr}|_{lin.} \cdot r + \frac{1}{2} e_{ss}|_{lin.} \cdot s + e_{rs}|_{bil.} \cdot rs \quad (23a)$$

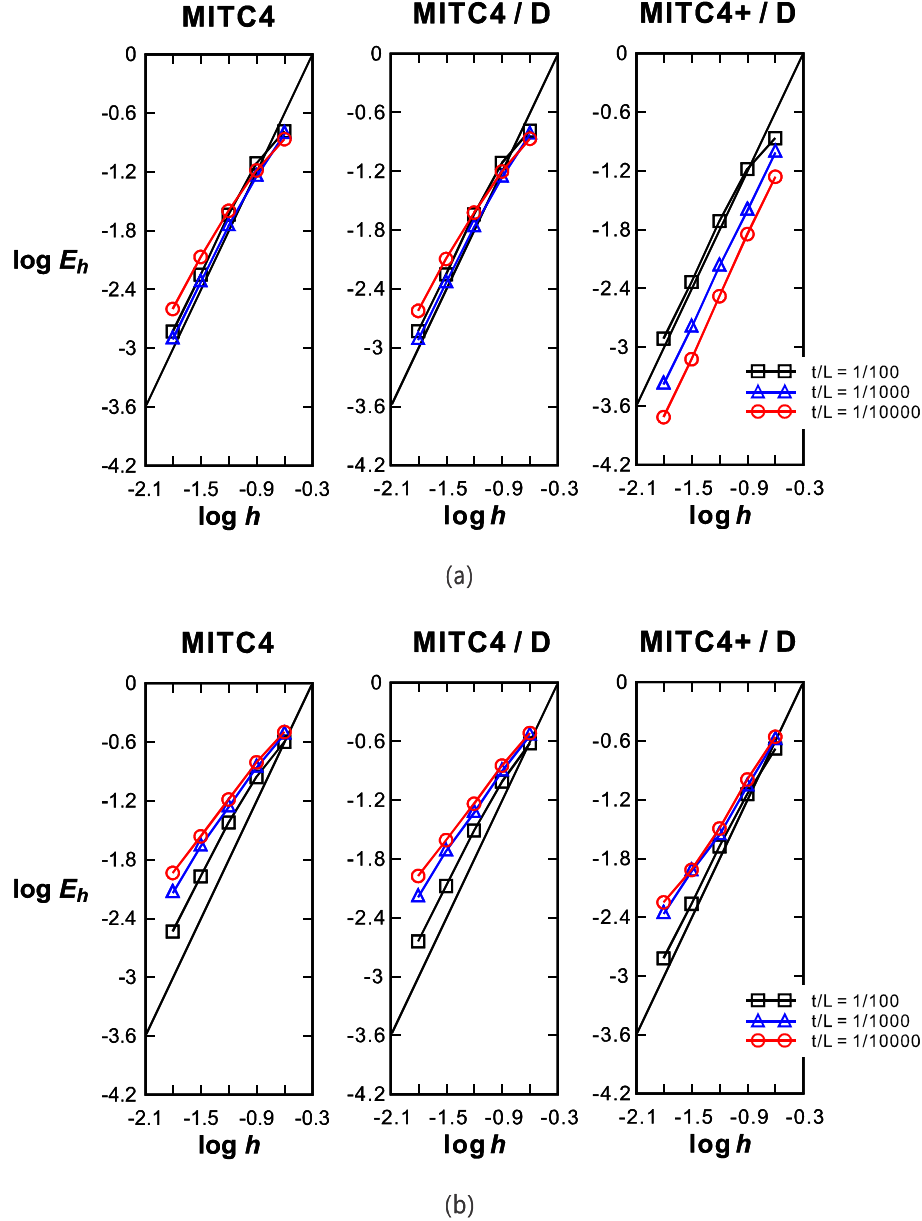


Fig. 15. Convergence curves for the clamped hyperboloid shell problem with (a) the graded regular and (b) distorted meshes. The bold line represents the optimal convergence rate.

with

$$\begin{aligned} e_{rr}|_{\text{con.}} &= \mathbf{x}_r \cdot \mathbf{u}_r, e_{ss}|_{\text{con.}} = \mathbf{x}_s \cdot \mathbf{u}_s, e_{rs}|_{\text{con.}} = \frac{1}{2} (\mathbf{x}_r \cdot \mathbf{u}_s + \mathbf{x}_s \cdot \mathbf{u}_r), \\ e_{rr}|_{\text{lin.}} &= \mathbf{x}_r \cdot \mathbf{u}_d + \mathbf{x}_d \cdot \mathbf{u}_r, e_{ss}|_{\text{lin.}} = \mathbf{x}_s \cdot \mathbf{u}_d + \mathbf{x}_d \cdot \mathbf{u}_s, e_{rs}|_{\text{bil.}} = \mathbf{x}_d \cdot \mathbf{u}_d \end{aligned} \quad (23b)$$

For the MITC4+ shell element (that is, not considering yet the drilling effect) the membrane strain is assumed to have the form

$$\tilde{e}_{ij}^m = a_0|_{ij} e_{rr}^m + a_1|_{ij} e_{rr}^{m(A)} + a_2|_{ij} e_{ss}^{m(B)} + a_3|_{ij} e_{ss}^{m(C)} + a_4|_{ij} e_{ss}^{m(D)} + a_5|_{ij} e_{rs}^{m(E)} \quad (24a)$$

and we use the following two assumptions to improve the element behavior, specifically to alleviate membrane-locking:

$$\begin{aligned} \bar{e}_{rr}^m &= e_{rr}^m(0, 0) + \frac{\sqrt{3}}{2} \lambda(r, s) (\bar{e}_{rr}^{m(\bar{A})} - \bar{e}_{rr}^{m(\bar{B})}) s, \\ \bar{e}_{ss}^m &= e_{ss}^m(0, 0) + \frac{\sqrt{3}}{2} \lambda(r, s) (\bar{e}_{ss}^{m(\bar{C})} - \bar{e}_{ss}^{m(\bar{D})}) r, \bar{e}_{rs}^m = e_{rs}^m(0, 0) \end{aligned} \quad (24b)$$

with $\lambda(r, s) = \frac{j_0}{j}(r, s, 0)$ and the tying points shown in Fig. 6. Then we

obtain

$$\begin{aligned} \tilde{e}_{rs}^m|_{\text{bil.}} &= \frac{c_r}{d} [c_r (e_{rr}^m|_{\text{con.}} + e_{rs}^m|_{\text{bil.}}) - e_{rr}^m|_{\text{lin.}}] + \frac{c_s}{d} [c_s (e_{ss}^m|_{\text{con.}} + e_{rs}^m|_{\text{bil.}}) \\ &\quad - e_{ss}^m|_{\text{lin.}}] + \frac{2c_r c_s}{d} e_{rs}^m|_{\text{con.}} \end{aligned} \quad (24c)$$

$c_r = \mathbf{x}_d \bar{\mathbf{g}}^T|_{(r,s,0)}$, $c_s = \mathbf{x}_d \bar{\mathbf{g}}^T|_{(r,s,0)}$, $d = c_r^2 + c_s^2 - 1$. Eq. (24b) improves the membrane behavior, and Eq. (24c) improves the bending part of the shell behavior by eliminating membrane locking.

The constants $a_k|_{ij}$ with $k = 0, 1, 2, 3, 4$, and 5 are given by

$$\begin{bmatrix} \tilde{e}_{rr}^m \\ \tilde{e}_{ss}^m \\ \tilde{e}_{rs}^m \end{bmatrix} = \mathbf{Q}(r, s) \mathbf{R}(r, s) \mathbf{S} \begin{bmatrix} e_{rr}^{m(A)} & e_{rr}^{m(B)} & e_{ss}^{m(C)} & e_{ss}^{m(D)} & e_{rs}^{m(E)} \end{bmatrix}^T \quad (25a)$$

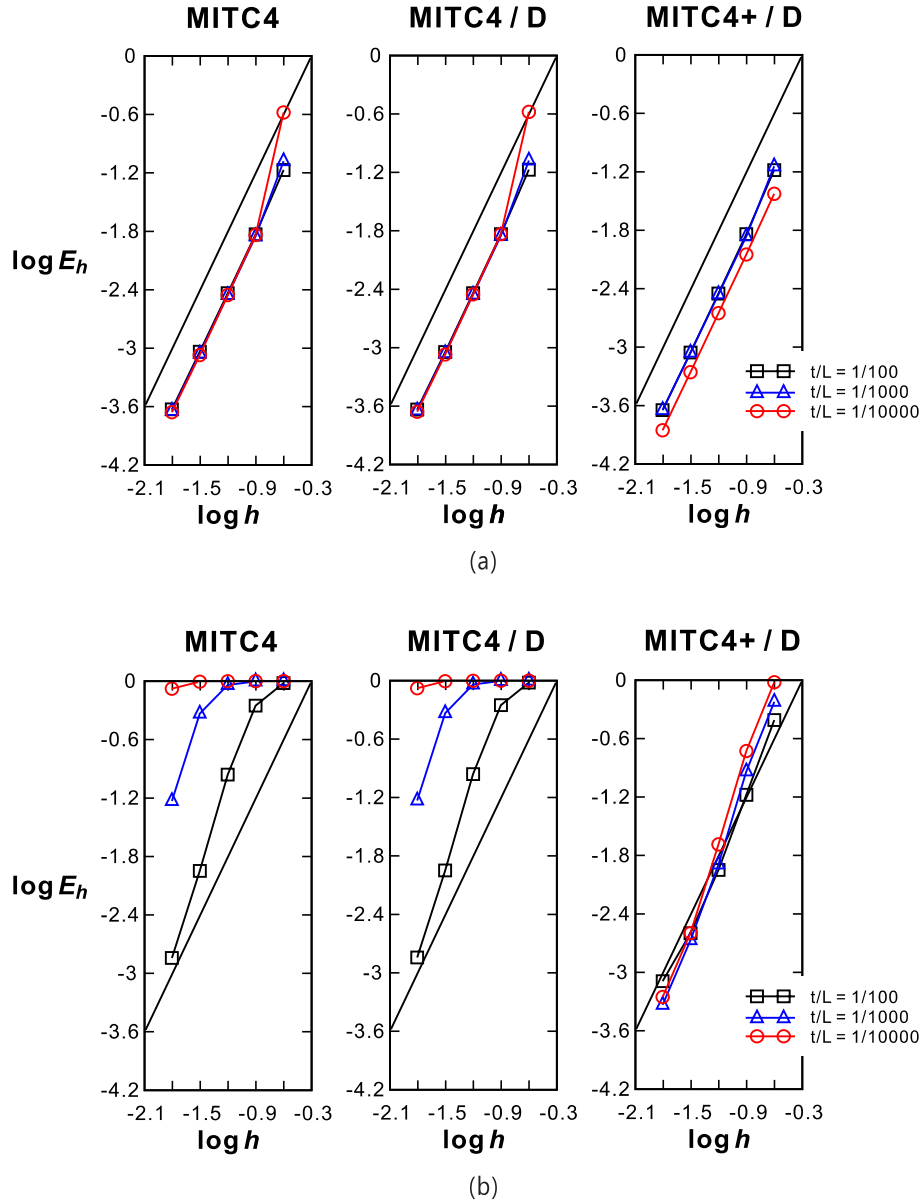


Fig. 16. Convergence curves for the free hyperboloid shell problem with (a) the graded regular and (b) distorted meshes. The bold line represents the optimal convergence rate.

$$\begin{bmatrix} a_0|_{rr} & a_1|_{rr} & a_2|_{rr} & a_3|_{rr} & a_4|_{rr} \\ a_0|_{ss} & a_1|_{ss} & a_2|_{ss} & a_3|_{ss} & a_4|_{ss} \\ a_0|_{rs} & a_1|_{rs} & a_2|_{rs} & a_3|_{rs} & a_4|_{rs} \end{bmatrix} = \mathbf{Q}(r,s)\mathbf{R}(r,s)\mathbf{S} \quad (25b)$$

$$\mathbf{Q}(r,s) = \begin{bmatrix} (1+c_r s)^2 & (c_s s)^2 & 2c_s s(1+c_r s) \\ (c_r r)^2 & (1+c_s r)^2 & 2c_r r(1+c_s r) \\ c_r r(1+c_r s) & c_s s(1+c_s r) & c_r c_s r s + (1+c_r s)(1+c_s r) \end{bmatrix}$$

$$\mathbf{R}(r,s) = \lambda \begin{bmatrix} 1/\lambda + \sqrt{3}n_1 s & \sqrt{3}n_2 s & 2\sqrt{3}n_5 s & n_3 s & n_4 s & n_1 s/\sqrt{3} \\ \sqrt{3}m_2 r & 1/\lambda + \sqrt{3}m_1 r & 2\sqrt{3}m_5 r & m_4 r & m_3 r & m_1 r/\sqrt{3} \\ 0 & 0 & 1/\lambda & 0 & 0 & 0 \end{bmatrix}$$

$$\mathbf{S} = \begin{bmatrix} 1/2 - a_A & 1/2 - a_B & -a_C & -a_D & -a_E \\ -a_A & -a_B & 1/2 - a_C & 1/2 - a_D & -a_E \\ 0 & 0 & 0 & 0 & 1 \\ 1/2 & -1/2 & 0 & 0 & 0 \\ 0 & 0 & 1/2 & -1/2 & 0 \\ a_A & a_B & a_C & a_D & a_E \end{bmatrix} \quad (25c)$$

$$a_A = \frac{c_r(c_r-1)}{2d}, a_B = \frac{c_r(c_r+1)}{2d}, a_C = \frac{c_s(c_s-1)}{2d}, a_D = \frac{c_s(c_s+1)}{2d}, a_E = \frac{2c_r c_s}{d},$$

$$\begin{aligned} n_1 &= \frac{1}{2} \left[(g_r^r)^2 \Big|_{(\bar{A})} - (g_r^r)^2 \Big|_{(\bar{B})} \right], n_2 = \frac{1}{2} \left[(g_s^r)^2 \Big|_{(\bar{A})} - (g_s^r)^2 \Big|_{(\bar{B})} \right], \\ n_3 &= \frac{1}{2} \left[(g_r^s)^2 \Big|_{(\bar{A})} + (g_r^s)^2 \Big|_{(\bar{B})} \right], \\ n_4 &= \frac{1}{2} \left[(g_r^r g_s^r) \Big|_{(\bar{A})} + (g_r^r g_s^r) \Big|_{(\bar{B})} \right], n_5 = \frac{1}{2} \left[(g_s^r g_s^s) \Big|_{(\bar{A})} - (g_s^r g_s^s) \Big|_{(\bar{B})} \right], \\ m_1 &= \frac{1}{2} \left[(g_s^s)^2 \Big|_{(\bar{C})} - (g_s^s)^2 \Big|_{(\bar{D})} \right], m_2 = \frac{1}{2} \left[(g_s^r)^2 \Big|_{(\bar{C})} - (g_s^r)^2 \Big|_{(\bar{D})} \right], \\ m_3 &= \frac{1}{2} \left[(g_s^s)^2 \Big|_{(\bar{C})} + (g_s^s)^2 \Big|_{(\bar{D})} \right], \\ m_4 &= \frac{1}{2} \left[(g_s^r g_s^s) \Big|_{(\bar{C})} + (g_s^r g_s^s) \Big|_{(\bar{D})} \right], m_5 = \frac{1}{2} \left[(g_s^r g_s^s) \Big|_{(\bar{C})} - (g_s^r g_s^s) \Big|_{(\bar{D})} \right] \end{aligned} \quad (25d)$$

The matrices \mathbf{Q} , \mathbf{R} , and \mathbf{S} respectively arise from the transformation of the strain components. The coefficients require only few bases to be calculated, and the computation is performed only once per element, see Appendix B.

We note that the expressions in Eq. (24) include the improvements proposed in Ref. [8] for the MITC4+ element presented in Refs. [5,7].

By adding the drill-membrane strain given in Eq. (21), we obtain the

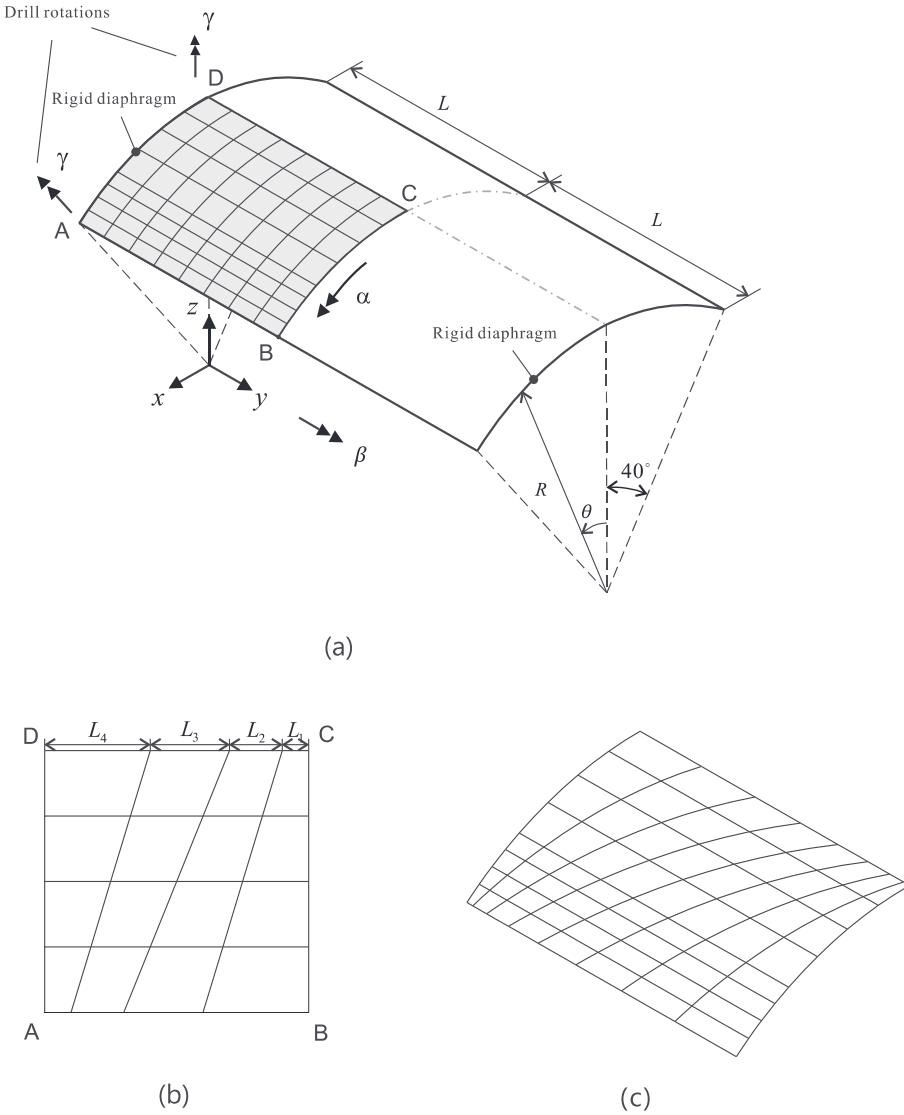


Fig. 17. Scordelis-Lo shell problem ($E = 4.32 \times 10^8$, $\nu = 0.0$, $R = 25.0$, $L = 25.0$ and self-weight = 90 per unit surface area). (a) Problem description with graded regular mesh (8 × 8 mesh). (b) Distorted mesh pattern (4 × 4 mesh). (c) Distorted mesh applied (8 × 8 mesh).

element denoted as ‘MITC4+ / D’.

$$e_{ij} = \tilde{e}_{ij}^m + e_{ij}^{md} + t e_{ij}^{b1} + t^2 e_{ij}^{b2} \quad \text{with } i, j = 1, 2 \quad (26)$$

In the above sections, we presented the elements for linear analyses. The formulations can directly be extended to nonlinear analyses using the procedures given in Ref. [4]. There is only a special consideration on how the total strain from the drill rotation can be measured and introduced. Without using the nonlinear terms in the strain terms, we can use the linear part of the strain given in Eqs. (19) and (21) but we need to accumulate the total drill rotation using always the instantaneous direction (\mathbf{v}^D) to obtain the total drill-strain (e_{ij}^{md}) corresponding to the total deformation.

We should also note that the above interpolation used for the MITC4+ shell element might appear rather complicated when in fact it is reasonably straight-forward in application. However, of course, related research efforts may be pursued to simplify the formulation, see for example Ref. [36], but then also the drill degree-of-freedom needs to be embedded in an effective way.

3. Numerical Assessments

In this section we first discuss that the new MITC4/D and MITC4+/D elements pass the basic tests (including the patch tests) and then, to indicate the capabilities of the MITC4/D element, we give the results of some illustrative planar beam solutions. These studies are followed by the evaluation of the new MITC4/D and MITC4+/D elements in shell linear analyses, as advocated in refs. [1,4,5]. Finally, we give some results of nonlinear analyses. We note that the elements require only the 2×2 Gauss integration over the element surfaces.

In some analyses, we compare the performance of the elements with the performance of the MITC4 element including incompatible modes, see Ref. [4], which we call the MITC4-IC element.

All MITC elements presented in this paper and used in the solutions below have been implemented in ADINA, version 24.0 of Bentley Systems, Inc. [21].

3.1. Basic tests including the patch tests

MITC/D and MITC4+/D elements pass the spatial isotropy test. The elements pass the zero energy mode tests, and rigid body modes are properly represented.

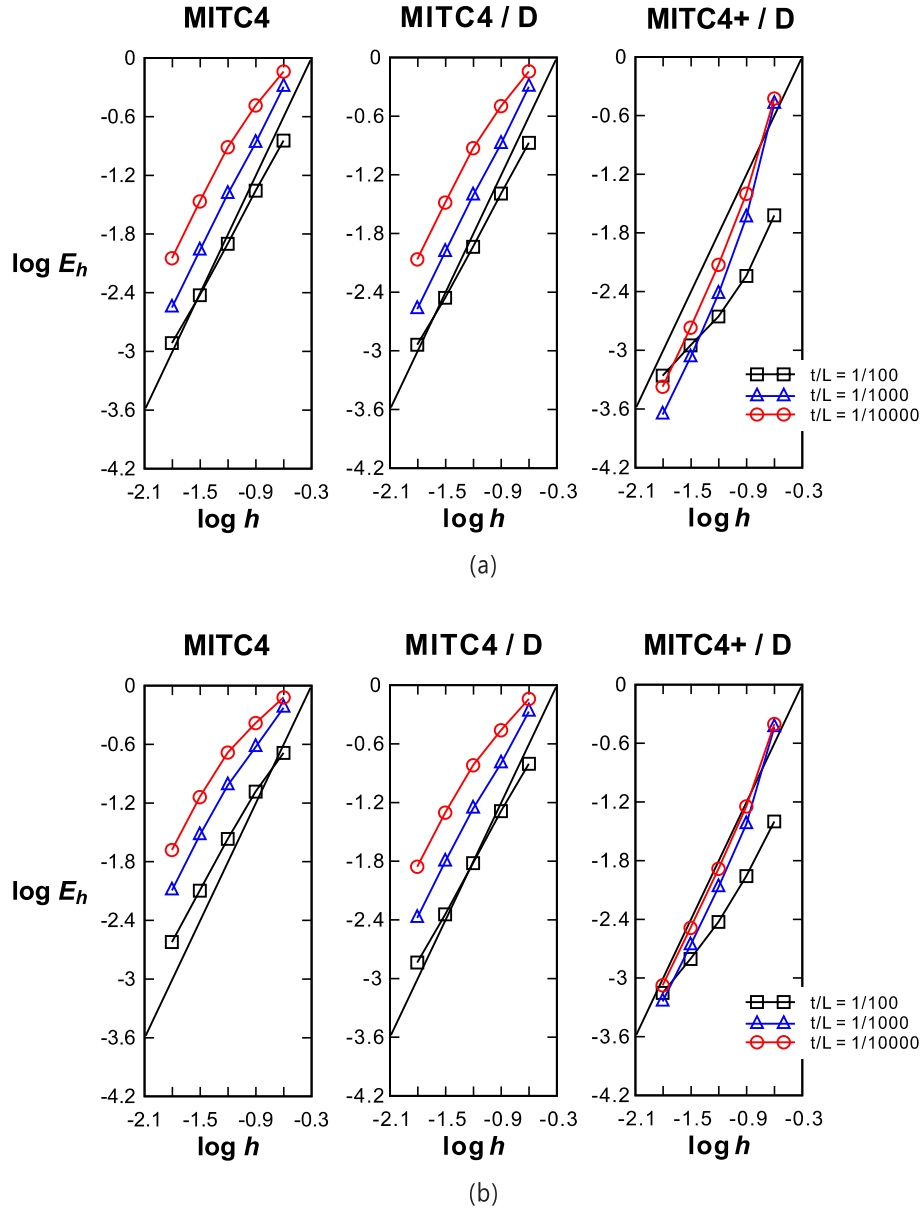


Fig. 18. Convergence curves for the Scordelis-Lo shell problem with (a) the regular and (b) distorted meshes. The bold line represents the optimal convergence rate.

The patch tests are shown in Fig. 7. We consider the ‘strong form’ of the patch tests [5,6,22,23], i.e. we require that the calculations give the analytical solutions of constant and zero stresses throughout the patch due to the applied loading. When considering the patch tests, it is important that the ‘minimum boundary conditions’ are imposed to constrain the patch from undergoing a rigid body motion. For each test, the solution should then be the constant straining mode.

Fig. 7 shows in detail what boundary conditions are imposed when including the drill degree of freedom θ_z at the nodes for the extension, bending, and shearing tests. We note that in all cases θ_z is left free at the element nodes except at the corner node B.

It is important that this strict form of the patch tests is performed, and for the elements presented all tests are strictly passed. Also, the use of $\theta_z = 0$ at the corner node C does not affect the results.

3.2. Illustrative solutions of 2D planar beam problems

We briefly show the in-plane performance of the MITC4/D element when compared to the use of the MITC4 and MITC4-IC elements. In all

problem solutions, using the MITC4/D and MITC4+/D shell elements the drill rotation is left free except at the edges with prescribed displacement boundary conditions. The reference solutions have been calculated using Reissner beam theory.

First, we solve for the response of a straight slender cantilever beam and consider a regular mesh and a distorted mesh of elements, see Fig. 8 [12,24,25]. The results are given in Table 1 and show that the MITC4/D and MITC4+/D elements perform quite well when using Mesh type 1 also compared to the performance of the MITC4-IC element, but all elements would need to be used with a much finer mesh when employing Mesh type 2.

Next, we solve for the response of a thick curved cantilever beam, see Fig. 9 [8,25,26]. The resulting displacements are given in Table 2 and again the MITC4/D and MITC4+/D elements perform well.

Finally, we consider the response of the thick cantilever in Fig. 10 [12,18,22,25] and use regular and distorted meshes for the analysis. The results are presented in Table 3 and here too, good response predictions are observed using the MITC4/D and MITC4+/D elements.

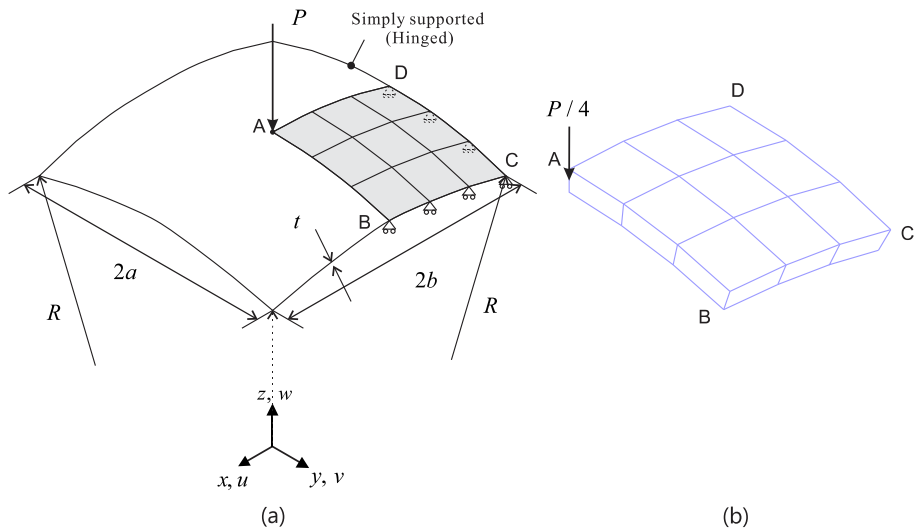


Fig. 19. Hinged spherical shell problem ($E = 68.95$, $\nu = 0.3$, $R = 2540$, $a = b = 784.9$ and $t = 99.45$). (a) Problem description. (b) Mesh used (3×3 mesh).

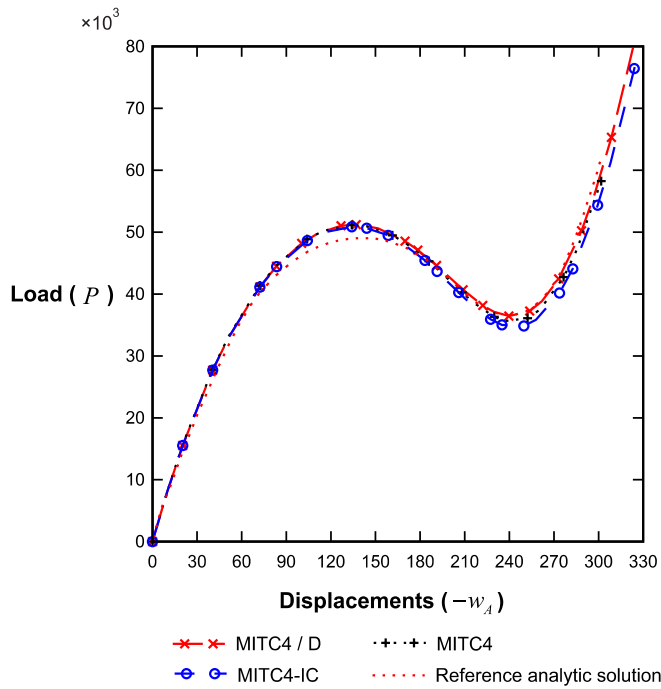


Fig. 20. Load-displacement curves for the hinged spherical shell problem.

3.3. Convergence in solutions of linear shell problems

As discussed previously, see Ref. [1–5], a mathematical convergence analysis of shell elements directed to solving general shell structures is out of reach. Hence numerical tests need to be performed and these tests should be well-designed and “all-encompassing” considering membrane dominated, bending-dominated and mixed shell behaviors.

In the MITC4/D and MITC4+/D formulations using the drill degree of freedom, the “drill-membrane strain” can enhance the element behavior in membrane and mixed membrane/bending dominated conditions.

The shell structural analysis problems we consider below are all-encompassing in behavior [1–5,27–29].

An important point is that a proper error norm needs to be used to measure the convergence. We use the s-norm proposed by Hiller and Bathe [27].

$$\|\mathbf{u} - \mathbf{u}_h\|_s^2 = \int_{\Omega} \Delta \boldsymbol{\epsilon}^T \Delta \boldsymbol{\tau} d\Omega \text{ with } \Delta \boldsymbol{\epsilon} = \boldsymbol{\epsilon} - \boldsymbol{\epsilon}_h, \Delta \boldsymbol{\tau} = \boldsymbol{\tau} - \boldsymbol{\tau}_h \quad (27)$$

where \mathbf{u} is the exact solution, \mathbf{u}_h is the solution of the finite element discretization, and $\boldsymbol{\epsilon}$ and $\boldsymbol{\tau}$ are the strain and stress vectors. This is a proper norm for investigating whether a finite element formulation satisfies the consistency and inf-sup conditions [1,27,28].

Since an analytical solution is generally not available, an accurate finite element solution using a very fine mesh \mathbf{u}_{ref} is used instead. Hence the s-norm is modified to be,

$$\|\mathbf{u}_{ref} - \mathbf{u}_h\|_s^2 = \int_{\Omega_{ref}} \Delta \boldsymbol{\epsilon}^T \Delta \boldsymbol{\tau} d\Omega_{ref} \text{ with } \Delta \boldsymbol{\epsilon} = \boldsymbol{\epsilon}_{ref} - \boldsymbol{\epsilon}_h, \Delta \boldsymbol{\tau} = \boldsymbol{\tau}_{ref} - \boldsymbol{\tau}_h. \quad (28)$$

To study the solution convergence of shell finite elements with decreasing thicknesses, we use the normalized relative error E_h

$$E_h = \frac{\|\mathbf{u}_{ref} - \mathbf{u}_h\|_s^2}{\|\mathbf{u}_{ref}\|_s^2} \quad (29)$$

The theoretical convergence behavior, which corresponds to the optimal convergence, is given by

$$E_h \cong Ch^k \quad (30)$$

in which C is a constant independent of the shell thickness t and h is the element size. For 4-node shell elements, $k = 2$.

In the testing, we use decreasing shell thicknesses and study the solution error measured in the s-norm to identify whether the discretization scheme gives a close to optimal performance, that is, the error is close to independent of the shell thickness and close to the value in Eq. (30). The rotational boundary conditions are either applied in the global system or in the local system using (α, β, γ) , as indicated in the description of the problems.

3.3.1. Cylindrical shell problem

We solve the cylindrical shell problem described in Fig. 11 (a) [1,2,3,28]. This shell structure has a single curvature and shows two different asymptotic behaviors depending on the boundary conditions at its ends: bending-dominated behavior when both ends are free and membrane-dominated behavior when both ends are clamped.

The loading is a smoothly varying pressure $p(\theta)$ (Fig. 11(b))

$$p(\theta) = p_0 \cos(2\theta) \quad (31)$$

Using symmetry, only the region ABCD in Fig. 11(a) is modeled. For the

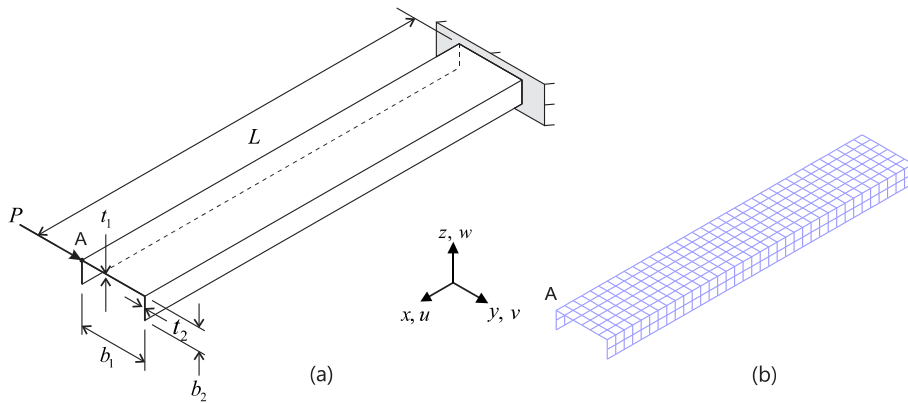


Fig. 21. Channel section beam problem, for the short channel section beam, $E = 1.0 \times 10^7$, $\nu = 0.333$, $L = 36$, $b_1 = 6$, $b_2 = 2$, $t_1 = t_2 = 0.05$. For the long channel section beam, $E = 21000$, $\nu = 0.3$, $L = 900$, $b_1 = 30$, $b_2 = 10$, $t_1 = 1$ and $t_2 = 1.6$. (a) Problem description. (b) Mesh used for short channel problem case.

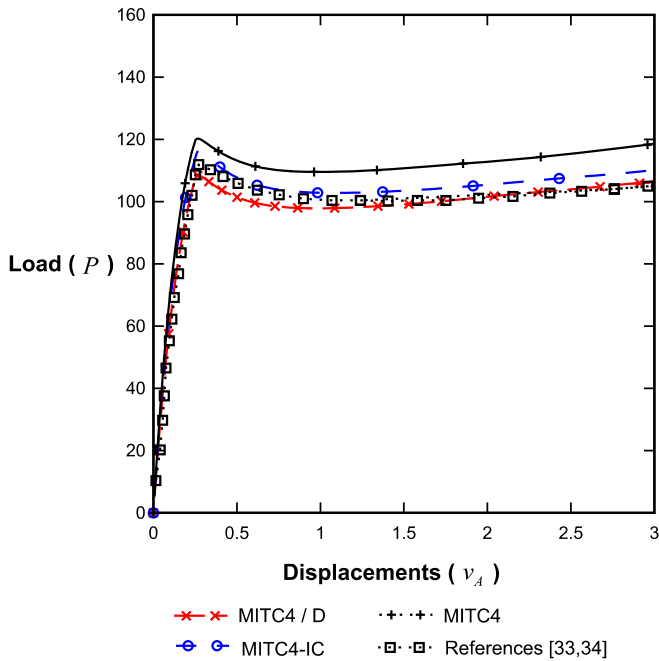


Fig. 22. Load-displacement curves for the short channel section beam problem.

bending-dominated and membrane-dominated cases, the boundary conditions are $u_x = \alpha = \gamma = 0$ along BC, $u_y = \beta = \gamma = 0$ along DC, and $u_z = \beta = \gamma = 0$ along AB. In addition, all degrees of freedom along AD are left free for the free boundary condition case and set to zero for the clamped boundary condition case.

Considering the clamped boundary condition, the regular mesh is graded with a boundary layer of width $2\sqrt{t}$, see Refs. [1,3] for details. In the free boundary condition, the graded mesh with a boundary layer of width $0.5\sqrt{t}$ is considered [1]. We also perform the convergence studies with the distorted meshes shown in Fig. 11(c), where each edge is discretized in the following ratio: $L_1:L_2:L_3: \dots :L_N = 1:2:3:\dots:N$ for $N \times N$ element mesh (Fig. 14 (b)).

The solutions are obtained with $N \times N$ element meshes ($N = 4, 8, 16, 32$ and 64). The element size is $h = L/N$. The reference solutions are calculated using a 72×72 element undistorted mesh of MITC9 shell elements.

Figs. 12 and 13 give the convergence curves in the solution of the cylindrical shell problems with clamped and free boundary conditions, respectively. All elements perform well in the clamped case using the regular or distorted meshes. However, while all elements also perform

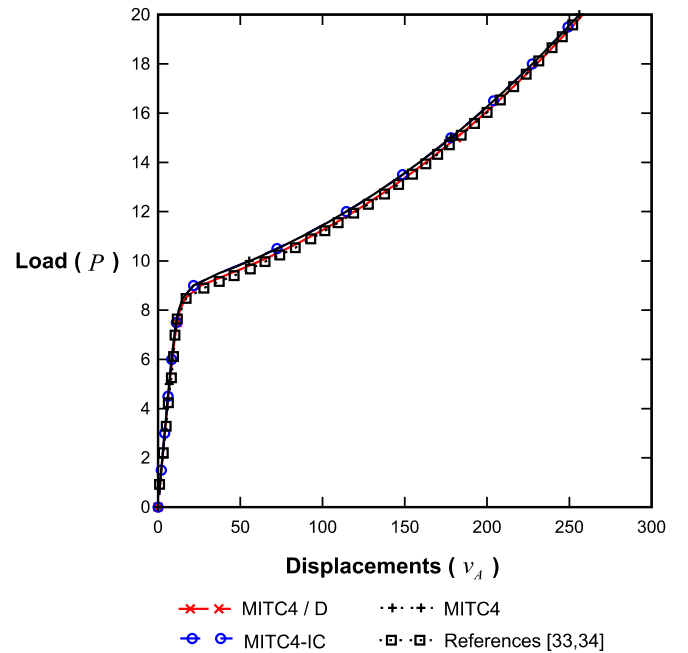


Fig. 23. Load-displacement curves for the long channel section beam problem.

well in the problem free case with the regular mesh, when using the distorted mesh, only the MITC4+/D shell element shows a close to optimal convergence behavior.

3.3.2. Hyperboloid shell problems

An important problem to solve is the hyperboloid shell problem shown in Fig. 14 (a) [1,5,27,31] because the structure has two and opposing curvatures. The mid-surface of the shell structure is given by $x^2 + z^2 = 1 + y^2; y \in [-1, 1]$. (32)

We apply the pressure loading used already above, given in Eq. (31). The structure is bending-dominated when free along the boundary AB and membrane-dominated when fixed along AB.

Using again symmetry, one-eighth of the structure corresponding to the shaded region ABCD in Fig. 14(a) is modeled for the analysis. We test the elements in the bending-dominated case with the boundary conditions $u_z = \beta = \gamma = 0$ along BC, $u_x = \beta = \gamma = 0$ along AD, and $u_y = \alpha = \gamma = 0$ along DC and all degrees free along AB. For the membrane-dominated case, the same boundary conditions are used along the symmetry lines, but the clamped boundary condition is imposed using

MITC4 / D

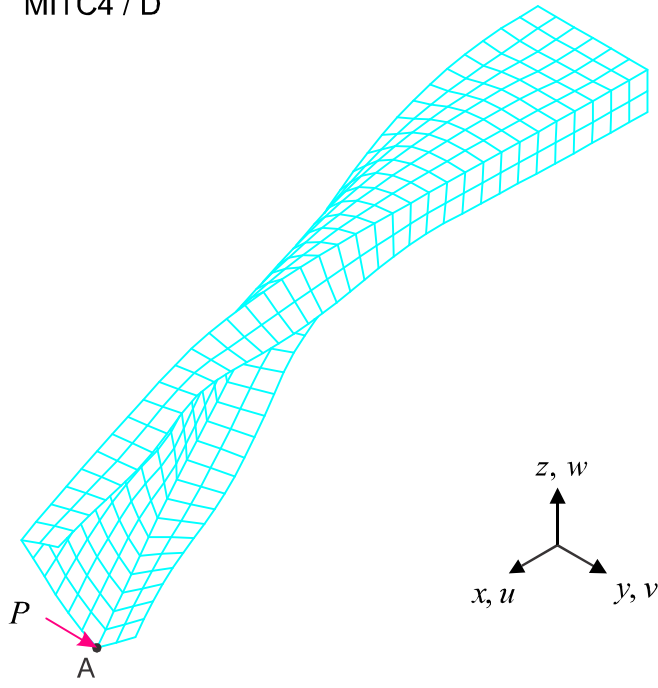


Fig. 24. Deformed shapes for the short channel-section beam when using the MITC4 / D element for the solution.

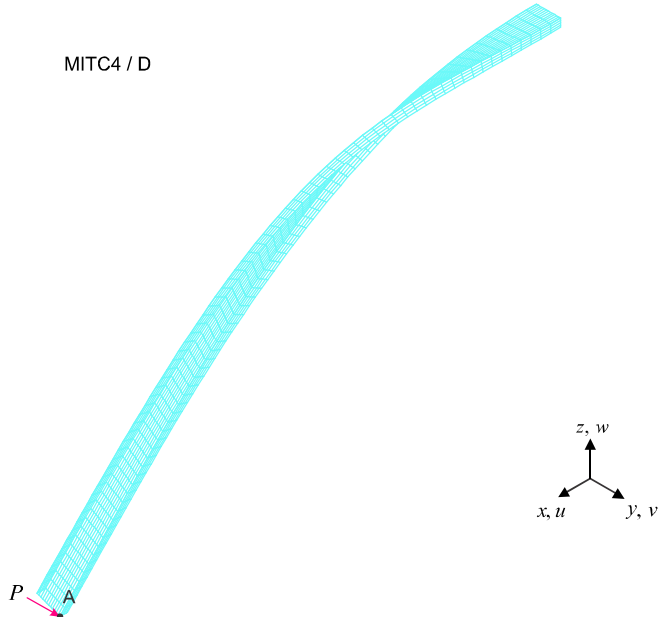


Fig. 25. Deformations of the long channel-section beam using the MITC4 / D element for the solution.

$$u_x = u_y = u_z = \alpha = \beta = \gamma = 0 \text{ along AB.}$$

The solutions are calculated using $N \times N$ element meshes ($N = 4, 8, 16, 32$ and 64). The element size is $h = L/N$. A 72×72 element mesh of undistorted MITC9 shell elements is used to obtain the reference solutions.

We use again a regular mesh and a distorted mesh. With the regular mesh, we grade the mesh of width $0.5\sqrt{t}$ for the free boundary condition and $6\sqrt{t}$ for the clamped boundary condition [1,27,31]. Using the distorted mesh, we apply the distortion pattern in Fig. 14(c), where for the $N \times N$ element mesh, each edge is discretized in the ratio $L_1:L_2:L_3: \dots$

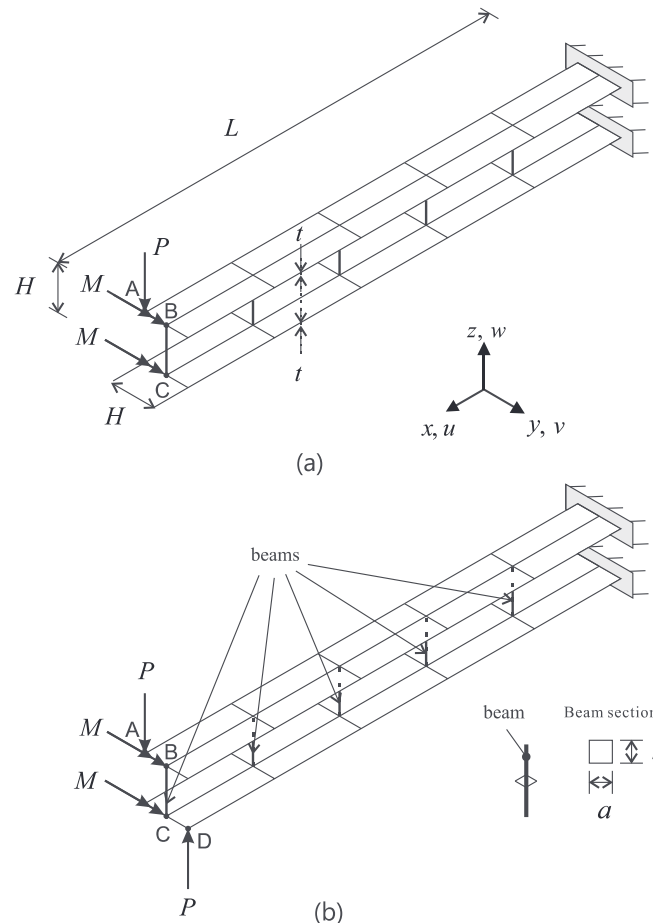


Fig. 26. An ad-hoc structure of two plates modeled with a very coarse idealization ($E = 2.1 \times 10^5$, $\nu = 0.0$, $L = 20$, $H = 2$ and $t = 0.1$). The plates are each subjected to the end-moment M , are connected by five beam elements ($a = b = 0.1$, $E = 2.1 \times 10^8$, $G = 1.05 \times 10^8$) and are also subjected to the corner tip loads P as shown (magnitude of $P = MH/2$). Since the plates undergo large displacements, see Fig. 27, we need to use shell elements to model the plates.

$$L_N = 1: 2: 3: \dots: N, \text{ see Fig. 14(d).}$$

Fig. 15 Shows the convergence of the solutions considering the clamped hyperboloid shell problem. All elements perform well in both mesh configurations

Fig. 16 gives the results considering the free hyperboloid shell problem. When the non-distorted mesh is used, all elements perform well. However, using the distorted mesh, only the MITC4+/D shows close to optimal behavior.

3.3.3. A shell problem with mixed membrane-bending actions

We consider the Scordelis-Lo shell shown in Fig. 17(a), see Refs. [6,8,19,29,30]. The shell is supported by rigid diaphragms at the ends and is free along the longitudinal edges which induces mixed membrane-bending behavior in the shell interior. This behavior corresponds in essence to a superposition of the membrane- and bending-dominant behaviors seen in the elliptical shell problems solved above.

Using symmetry, only the shaded region ABCD in Fig. 17(a) was modeled for analysis. The following boundary conditions are employed: $u_x = \beta = \gamma = 0$ along DC, the condition of the rigid-diaphragm $u_x = u_z = \beta = 0$ along AD and the symmetry conditions $u_y = \alpha = \gamma = 0$ along BC. As load, self-weight in the u_z -direction was applied.

The solutions are calculated using $N \times N$ element meshes, with the distorted mesh patterns shown in Fig. 17(b) and 17(c). The use of the distorted meshes substantially tests, in particular, the performance of the shell elements. A non-distorted mesh of 72×72 MITC9 shell

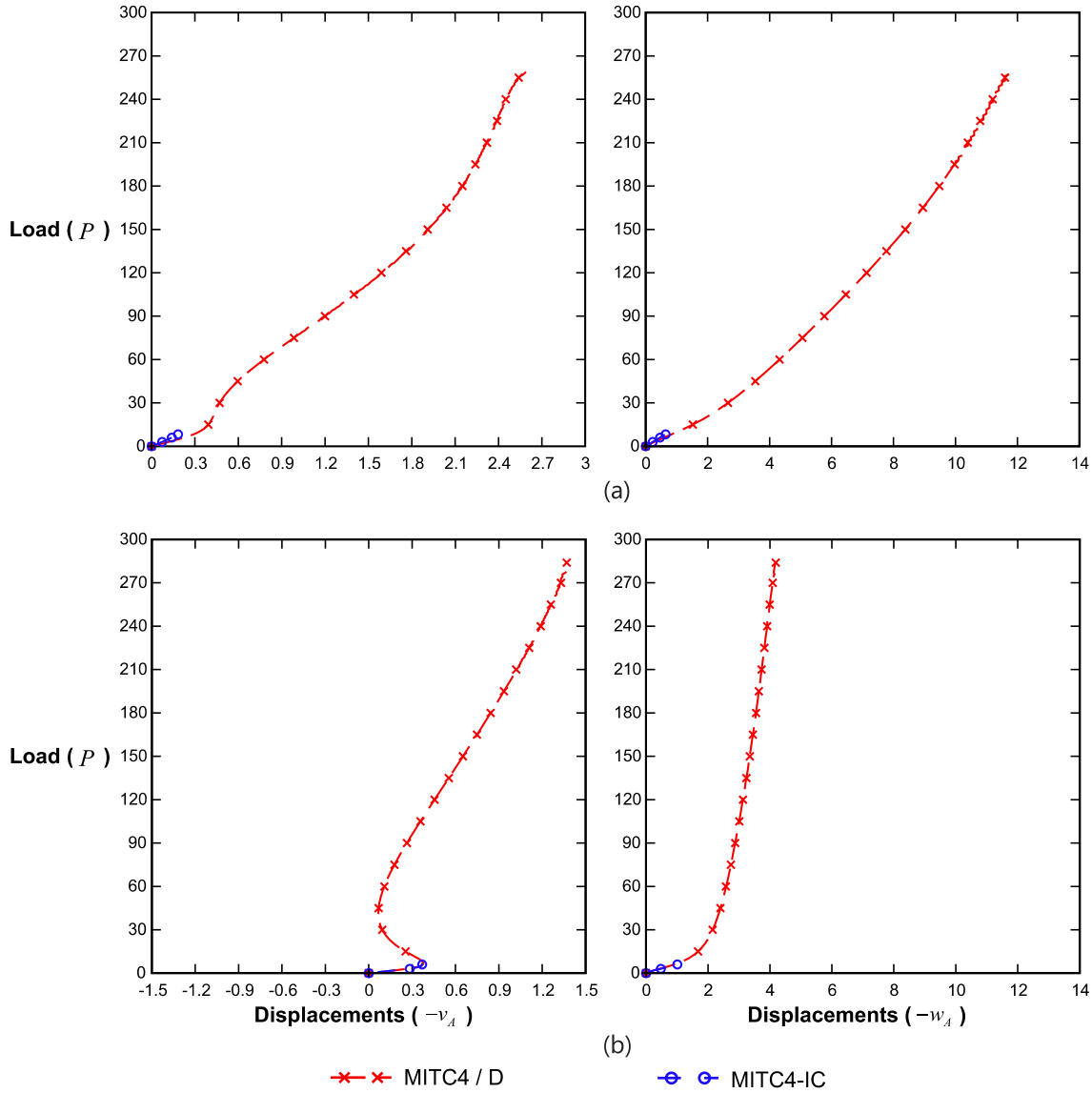


Fig. 27. Load-displacement curves for the ad-hoc problems of Fig. 26. (a) Load case in Fig. 26(a). (b) Load case in Fig. 26(b).

elements was used to obtain the reference solution.

Fig. 18 shows the convergence graphs of the elements used. The MITC4+/D element converges significantly better than the MITC4 element, and indeed also better than the shell elements earlier presented in Refs. [5,7,8].

3.4. Geometric nonlinear analyses

The purpose of this section is to illustrate the use of the elements in nonlinear analyses. In addition, we also illustrate how the elements can be used when intersecting shells need be modeled (like when analyzing a channel).

For the problems solved, the response predictions using the MITC4/D and MITC4+/D shell elements are almost identical.

3.4.1. Hinged spherical shell problem

We consider the hinged spherical shell problem in Fig. 19 [4,19]. Utilizing symmetry, only one-quarter of the structure corresponding to the shaded region ABCD in Fig. 19(a) is modeled for the analysis. The symmetry boundary conditions are imposed as $u_x = \theta_y = \theta_z = 0$ along AB and $u_y = \theta_x = \theta_z = 0$ along AD. The edges are simply supported with $u_x = u_y = u_z = 0$ along BC and DC. The drill degrees of freedom were not

restrained, and a very coarse mesh of 3×3 elements was used, see Fig. 19(b).

We required the analysis to find the load–displacement path and used the arc-length method or ‘Load-Displacement Control’ in ADINA [32]. The solutions were calculated until the downward displacement at point A exceeded the threshold value of 300. The analytical reference solution was furnished by Leichester [19].

Fig. 20 Shows the calculated load–displacement curves using the elements. It is remarkable that the solutions using all elements in this coarse mesh predict a response reasonably close to the reference solution

3.4.2. Channel section beam problems

We consider and solve the channel section beam problems referred to in Fig. 21 [33,34]. The beam can be either short or long. These cases are known to exhibit very different behaviors. The response of a short channel section beam is dominated by a local behavior (local buckling), while long channel section beams are dominated by a global behavior.

Fig. 22 presents the load–displacement curve of a short channel section beam compared to the solutions in Refs. [33,34] and Fig. 23 shows the load–displacement curve of a long channel section beam compared to the solutions in these references. The solutions obtained

using the MITC4/D element discretizations follow closely the earlier published results (and in Fig. 22 closer than when using the MITC4 shell element). The deformed shapes given in Fig. 24 and Fig. 25 show the presence of local and global buckling, as also displayed in Refs [33,34].

3.4.3. An ad hoc problem of shell to beam connection

merely to show the usefulness of the shell elements when beams need to be connected, see Fig. 26. Two parallel plates are modeled with meshes of 5×2 shell elements. Beam elements using all 6 degrees of freedom are connecting the plates along their centerlines. We use shell elements for the plate structures because large displacements are expected in the response. However, the finite element idealizations are rather coarse for this simple demonstration and we cannot expect high accuracy in the solutions.

We compare the response obtained using the MITC4/D and MITC4-IC elements where the MITC4-IC element formulation does not include the drill degrees of freedom and corresponding strain enhancements. Fig. 27 presents the load–displacement curves of the finite element models. Our new MITC4/D element with the drill degrees of freedom shows the full large displacement response without difficulties, whereas the model using the MITC4-IC element no longer converges at a relatively small load. In analyses only requiring five degrees of freedom at the nodes, the MITC4-IC element frequently performs better than the MITC4 element. However, in this case requiring six degrees of freedom at the nodes, as expected, the incompatible modes do not help in the response prediction.

4. Concluding remarks

We presented a further development of the quadrilateral MITC shell elements to include the drill rotational degree of freedom at the nodes. This solution feature can be important in the analysis of practical engineering problems.

The MITC4/D element includes the drill rotational degree of freedom in the widely used MITC4 element. A further development is the MITC4+/D shell element. Both element developments include the drilling stiffness using the fundamental scheme proposed by DJ Allman [10,11]. An important point, however, is that the MITC4/D and MITC4+/D elements are in general not of flat geometry and the bending

and membrane actions are fully coupled in their interiors. This interior coupling is important in general shell analyses [1].

The new elements pass all basic tests and provide stable solutions when used in the analysis of intersecting shells and when connected to beam elements. The elements employ all six standard degrees of freedom at the nodes, like used with beam elements.

While the use of the drilling degree of freedom provides in linear analysis an improvement in modeling features, the use of this degree of freedom can also be important in geometrically nonlinear analyses. We demonstrated the use of the new MITC4/D element in some nonlinear solutions, noting that the use of the MITC4+/D element gives in these analyses almost identical response predictions.

Considering future research, it would be valuable to study the performance of the MITC elements when used as “overlapping elements”, in particular, in the AMORE scheme, see Refs. [5,16,35]. Also, it may be effective to use the drill rotational degree of freedom only at certain nodes of the shell elements, namely only at those that connect shells to beams or at intersecting shells.

CRediT authorship contribution statement

Yeongbin Ko: Conceptualization, Data curation, Formal analysis, Investigation, Methodology, Project administration, Resources, Supervision, Validation, Writing – original draft, Writing – review & editing. **Klaus-Jürgen Bathe:** Conceptualization, Methodology, Supervision, Validation, Writing – review & editing. **Xinwei Zhang:** Investigation, Methodology, Software.

Declaration of competing interest

The authors declare that they have no known competing financial interests or personal relationships that could have appeared to influence the work reported in this paper.

Acknowledgment

We thank Dr. Jan Walczak of Bentley Systems, Inc. for sharing knowledge and insight on the analysis of shell problems in the industry.

Appendix A. Insight into the strain assumptions in Eq. (19)

We obtain further insight into the strain field of Eq. (19) by considering the derivation using the displacement-based strain and the MITC technique. Consider the drill-membrane strain

$$\begin{aligned} \tilde{e}_{rr}(\theta) &= \frac{j_0}{j} \left[\frac{1}{2}(1+s)\bar{e}_{rr}(\theta)|_{s=1} + \frac{1}{2}(1-s)\bar{e}_{rr}(\theta)|_{s=-1} \right] \\ \tilde{e}_{ss}(\theta) &= \frac{j_0}{j} \left[\frac{1}{2}(1+r)\bar{e}_{ss}(\theta)|_{r=1} + \frac{1}{2}(1-r)\bar{e}_{ss}(\theta)|_{r=-1} \right] \\ \tilde{e}_{rs}(\theta) &= \frac{1}{2} \frac{j_0}{j} \left[\frac{1}{2}(1+s)\bar{e}_{rs}(\theta)|_{s=1} + \frac{1}{2}(1-s)\bar{e}_{rs}(\theta)|_{s=-1} + \frac{1}{2}(1+r)\bar{e}_{rs}(\theta)|_{r=1} + \frac{1}{2}(1-r)\bar{e}_{rs}(\theta)|_{r=-1} \right] \end{aligned} \quad (\text{A.1})$$

with $s = 1, s = -1, r = 1$ and $r = -1$ corresponding to the ‘location of edges’ in Fig. 4(b), and $\frac{1}{2}(1+s), \frac{1}{2}(1-s), \frac{1}{2}(1+r)$ and $\frac{1}{2}(1-r)$ are respective functions at tied edges and $\frac{j_0}{j}$ is the volume ratio of the element domain.

We can show the equivalence of the strain in Eq. (18) (and Eq. (19d)) to the strain expressions in Eq. (A.1). The strain in Eq. (18) using the interpolation in Eq. (11) is expanded as

$$\begin{aligned}
\tilde{e}_{rr}^{md} &= \frac{j_0}{j} \tilde{h}_{m,r}^6 c_r^6 (-\theta_1^D + \theta_2^D) + \frac{j_0}{j} \tilde{h}_{m,r}^8 c_r^8 (-\theta_3^D + \theta_4^D) \\
\tilde{e}_{ss}^{md} &= \frac{j_0}{j} \tilde{h}_{m,s}^5 c_s^5 (\theta_4^D - \theta_1^D) + \frac{j_0}{j} \tilde{h}_{m,s}^7 c_s^7 (\theta_2^D - \theta_3^D) \\
\tilde{e}_{rs}^{md} &= \frac{1}{2} \frac{j_0}{j} \tilde{h}_{m,r}^6 c_s^6 (\theta_1^D - \theta_2^D) + \frac{1}{2} \frac{j_0}{j} \tilde{h}_{m,r}^8 c_s^8 (\theta_3^D - \theta_4^D) + \frac{1}{2} \frac{j_0}{j} \tilde{h}_{m,s}^5 c_r^5 (\theta_1^D - \theta_4^D) + \frac{1}{2} \frac{j_0}{j} \tilde{h}_{m,s}^7 c_r^7 (-\theta_2^D + \theta_3^D) \\
2\tilde{e}_{rs}^{md} + \tilde{e}_{rr}^{md} + \tilde{e}_{ss}^{md} &= 0
\end{aligned} \tag{A.2}$$

and

$$\begin{aligned}
\tilde{e}_{rr}^{md} &= \tilde{e}_{rr}^{md}|_{lin} \cdot r + \tilde{e}_{rr}^{md}|_{bilin} \cdot rs \\
\tilde{e}_{ss}^{md} &= \tilde{e}_{ss}^{md}|_{lin} \cdot s + \tilde{e}_{ss}^{md}|_{bilin} \cdot rs \\
\tilde{e}_{rs}^{md} &= -\frac{1}{2} \tilde{e}_{rr}^{md}|_{lin} \cdot r - \frac{1}{2} \tilde{e}_{ss}^{md}|_{lin} \cdot s - \frac{1}{2} (\tilde{e}_{rr}^{md}|_{bilin} + \tilde{e}_{ss}^{md}|_{bilin}) rs \\
\tilde{e}_{rr}^{md}|_{lin} &= \frac{j_0}{j} \frac{1}{2} [c_r^6 (\theta_1^D - \theta_2^D) + c_r^8 (\theta_3^D - \theta_4^D)] \\
\tilde{e}_{ss}^{md}|_{lin} &= \frac{j_0}{j} \frac{1}{2} [c_s^5 (-\theta_4^D + \theta_1^D) + c_s^7 (-\theta_2^D + \theta_3^D)] \\
\tilde{e}_{rr}^{md}|_{bilin} &= \frac{j_0}{j} \frac{1}{2} [c_r^6 (\theta_1^D - \theta_2^D) + c_r^8 (\theta_3^D - \theta_4^D)] \\
\tilde{e}_{ss}^{md}|_{bilin} &= \frac{j_0}{j} \frac{1}{2} [c_s^5 (-\theta_4^D + \theta_1^D) + c_s^7 (\theta_2^D - \theta_3^D)] \tag{A.3}
\end{aligned}$$

where we note that compared with the standard displacement-based membrane strain (e_{rr}^m and e_{ss}^m) in Eq. (23a), the new strain terms (\tilde{e}_{rr}^{md} and \tilde{e}_{ss}^{md}) add additional terms in r and s , respectively.

The strain in Eq. (A.1) is now expanded as follows. Using Eqs. (10), (17a) and substituting in Eq. (A.1), we obtain

$$\begin{aligned}
\tilde{e}_{rr}(\theta) &= \frac{j_0}{j} \left[\frac{1}{2} (1+s) h_{I,r} \Big|_{s=1} + \frac{1}{2} (1-s) h_{I,r} \Big|_{s=-1} \right] (\theta_{i+1}^D - \theta_i^D) \mathbf{x}_m^I \cdot (-\mathbf{x}_r^I \times \mathbf{V}^D) \\
\tilde{e}_{ss}(\theta) &= -\frac{j_0}{j} \left[\frac{1}{2} (1+r) h_{I,s} \Big|_{r=1} + \frac{1}{2} (1-r) h_{I,s} \Big|_{r=-1} \right] (\theta_{i+1}^D - \theta_i^D) \mathbf{x}_m^I \cdot (\mathbf{x}_s^I \times \mathbf{V}^D) \\
\tilde{e}_{rs}(\theta) &= -\frac{j_0}{j} \left[\frac{1}{4} h_{I,r} \Big|_{s=1} + \frac{1}{4} h_{I,r} \Big|_{s=-1} \right] (\theta_{i+1}^D - \theta_i^D) \mathbf{x}_m^I \cdot (\mathbf{x}_s^I \times \mathbf{V}^D) + \frac{j_0}{j} \left[\frac{1}{4} h_{I,s} \Big|_{r=1} + \frac{1}{4} h_{I,s} \Big|_{r=-1} \right] (\theta_{i+1}^D - \theta_i^D) \mathbf{x}_m^I \cdot (-\mathbf{x}_r^I \times \mathbf{V}^D) \tag{A.4}
\end{aligned}$$

which gives the strain Eq. (A.1) at the edges I . Then using Eq. (19c) we have

$$\begin{aligned}
\tilde{e}_{rr}(\theta) &= \frac{j_0}{j} [0 \quad (-r)(1+s) \quad 0 \quad (-r)(1-s)] \begin{bmatrix} c_r^5 (\theta_1^D - \theta_4^D) \\ c_r^6 (\theta_2^D - \theta_1^D) \\ c_r^7 (\theta_3^D - \theta_2^D) \\ c_r^8 (\theta_4^D - \theta_3^D) \end{bmatrix} \\
\tilde{e}_{ss}(\theta) &= -\frac{j_0}{j} [(-s)(1+r) \quad 0 \quad (-s)(1-r) \quad 0] \begin{bmatrix} c_s^5 (\theta_1^D - \theta_4^D) \\ c_s^6 (\theta_2^D - \theta_1^D) \\ c_s^7 (\theta_3^D - \theta_2^D) \\ c_s^8 (\theta_4^D - \theta_3^D) \end{bmatrix} \\
\tilde{e}_{rs}(\theta) &= -\frac{1}{2} [0 \quad (-r)(1+s) \quad 0 \quad (-r)(1-s)] \begin{bmatrix} c_s^5 (\theta_1^D - \theta_4^D) \\ c_s^6 (\theta_2^D - \theta_1^D) \\ c_s^7 (\theta_3^D - \theta_2^D) \\ c_s^8 (\theta_4^D - \theta_3^D) \end{bmatrix} + \frac{1}{2} [(-s)(1+r) \quad 0 \quad (-s)(1-r) \quad 0] \begin{bmatrix} c_r^5 (\theta_1^D - \theta_4^D) \\ c_r^6 (\theta_2^D - \theta_1^D) \\ c_r^7 (\theta_3^D - \theta_2^D) \\ c_r^8 (\theta_4^D - \theta_3^D) \end{bmatrix} \tag{A.5}
\end{aligned}$$

Therefore, $\tilde{e}_{ij}(\theta) = \tilde{e}_{ij}^{md}(\theta)$, which reveals the physical meaning of Eq. (11), namely that of tying strains at the element edges.

Appendix B. Computation of coefficients in Eq. (24)

From the definition of the coefficients δ_{ij}^j considering Fig. 6, we have

$$\begin{aligned} \mathbf{g}_r^r|_{(\bar{A})} &= \mathbf{x}_r \cdot \mathbf{g}^r|_{(0, \frac{1}{\sqrt{3}}, 0)} \mathbf{g}_r^s|_{(\bar{A})} = \mathbf{x}_r \cdot \mathbf{g}^s|_{(0, \frac{1}{\sqrt{3}}, 0)} \mathbf{g}_r^r|_{(\bar{B})} = \mathbf{x}_r \cdot \mathbf{g}^r|_{(0, -\frac{1}{\sqrt{3}}, 0)} \mathbf{g}_r^s|_{(\bar{B})} = \mathbf{x}_r \cdot \mathbf{g}^s|_{(0, -\frac{1}{\sqrt{3}}, 0)} \\ \mathbf{g}_s^r|_{(\bar{C})} &= \mathbf{x}_s \cdot \mathbf{g}^r|_{(-\frac{1}{\sqrt{3}}, 0, 0)} \mathbf{g}_s^s|_{(\bar{C})} = \mathbf{x}_s \cdot \mathbf{g}^s|_{(-\frac{1}{\sqrt{3}}, 0, 0)} \mathbf{g}_s^r|_{(\bar{D})} = \mathbf{x}_s \cdot \mathbf{g}^r|_{(-\frac{1}{\sqrt{3}}, 0, 0)} \mathbf{g}_s^s|_{(\bar{D})} = \mathbf{x}_s \cdot \mathbf{g}^s|_{(-\frac{1}{\sqrt{3}}, 0, 0)}. \end{aligned} \quad (\text{B.1})$$

Using Eq. (4b), and $\delta_{ij}^j = \mathbf{g}_r|_{(r,s,0)} \cdot \mathbf{g}^r|_{(r,s,0)}$, we obtain

$$\begin{aligned} \mathbf{x}_r \cdot \mathbf{g}^r|_{(0, \frac{1}{\sqrt{3}}, 0)} &= 1 - \frac{1}{\sqrt{3}} \mathbf{x}_d \cdot \mathbf{g}^r(0, \frac{1}{\sqrt{3}}, 0), \mathbf{x}_r \cdot \mathbf{g}^s|_{(0, \frac{1}{\sqrt{3}}, 0)} = -\frac{1}{\sqrt{3}} \mathbf{x}_d \cdot \mathbf{g}^s(0, \frac{1}{\sqrt{3}}, 0) = -\frac{c_s}{\sqrt{3}}, \\ \mathbf{x}_s \cdot \mathbf{g}^r|_{(-\frac{1}{\sqrt{3}}, 0, 0)} &= -\frac{1}{\sqrt{3}} \mathbf{x}_d \cdot \mathbf{g}^r(-\frac{1}{\sqrt{3}}, 0, 0) = -\frac{c_r}{\sqrt{3}}, \mathbf{x}_s \cdot \mathbf{g}^s|_{(-\frac{1}{\sqrt{3}}, 0, 0)} = 1 - \frac{1}{\sqrt{3}} \mathbf{x}_d \cdot \mathbf{g}^s(-\frac{1}{\sqrt{3}}, 0, 0), \end{aligned} \quad (\text{B.2})$$

where we used that $\mathbf{g}^r(a, 0, 0) = \mathbf{g}^r(0, 0, 0) = \mathbf{m}^r$ and $\mathbf{g}^s(0, a, 0) = \mathbf{g}^s(0, 0, 0) = \mathbf{m}^s$ for any a , and the coefficients $c_r = \mathbf{x}_d \cdot \bar{\mathbf{g}}^r|_{(r,s,0)} = \mathbf{x}_d \cdot \mathbf{m}^r$, $c_s = \mathbf{x}_d \cdot \bar{\mathbf{g}}^s|_{(r,s,0)} = \mathbf{x}_d \cdot \mathbf{m}^s$ in Eq. (24c).

Hence, only the following base vectors (and their conjugates) are required to determine all coefficients in Eq. (24)

$$\mathbf{x}_r, \mathbf{x}_s, \mathbf{x}_d, \mathbf{g}^r(0, \frac{1}{\sqrt{3}}, 0), \mathbf{g}^r(0, -\frac{1}{\sqrt{3}}, 0), \mathbf{g}^s(\frac{1}{\sqrt{3}}, 0, 0), \mathbf{g}^s(-\frac{1}{\sqrt{3}}, 0, 0)$$

Data availability

Data will be made available on request.

References

- [1] Chapelle D, Bathe KJ. The finite element analysis of shells - fundamentals. 2nd edition. Berlin: Springer; 2003. 2011.
- [2] Chapelle D, Bathe KJ. Fundamental considerations for the finite element analysis of shell structures. Comput Struct 1998;66(1): 19-36,711-2.
- [3] Bathe KJ, Iosilevich A, Chapelle D. An evaluation of the MITC shell elements. Comput Struct 2000;75(1):1-30.
- [4] Bathe KJ. Finite element procedures. Prentice Hall; 1996, 2nd ed. K.J. Bathe, Watertown, MA; 2014 and Higher Education Press, China; 2016.
- [5] Bathe KJ. Finite element procedures – *en plus*. Springer Verlag; 2025.
- [6] Dvorkin EN, Bathe KJ. A continuum mechanics based four-node shell element for general non-linear analysis. Engineering Comput 1984;1(1):77-88.
- [7] Ko Y, Lee PS, Bathe KJ. A new MITC4+ shell element. Comput Struct 2017;182: 404-18.
- [8] Ko Y, Lee PS, Bathe KJ. A new 4-node MITC element for analysis of two-dimensional solids and its formulation in a shell element. Comput Struct 2017;192: 34-49.
- [9] Ko Y, Lee PS, Bathe KJ. The MITC4+ shell element in geometric nonlinear analysis. Comput Struct 2017;185:1-14.
- [10] Allman DJ. A compatible triangular element including vertex rotations for plane elasticity analysis. Comput Struct 1984;19(1-2):1-8.
- [11] Allman DJ. A quadrilateral finite element including vertex rotations for plane elasticity analysis. Inter J Numer Meth Engrg 1988;26(3):717-30.
- [12] MacNeal RH, Harder RL. A refined four-noded membrane element with rotational degrees of freedom. Comput Struct 1988;28(1):75-84.
- [13] Hughes TJR, Brezzi F. On drilling degrees of freedom. Comput Meth Appl Mech Engrg 1989;72(1):105-21.
- [14] Ibrahimbegovic A, Wilson EL. A unified formulation for triangular and quadrilateral flat shell finite elements with six nodal degrees of freedom. Comm Appl Numer Meth. 1991;7(1):1-9.
- [15] Wisniewski K, Turska E. Enhanced Allman quadrilateral for finite drilling rotations. Comput Meth Appl Mech Engrg 2006;195(44-47):6086-109.
- [16] Lee S, Bathe KJ. An enhancement of overlapping finite elements. Comput Struct 2022;260:106704.
- [17] Lee S, Bathe KJ. Additional overlapping finite elements–The pyramid and prism elements. Comput Struct 2022;268:106813.
- [18] Cook RD. On the Allman triangle and a related quadrilateral element. Comput Struct 1986;22(6):1065-7.
- [19] Bathe KJ, Ho LW. A simple and effective element for analysis of general shell structures. Comput Struct 1981;13(5-6):673-81.
- [20] Lee PS, Bathe KJ. Insight into finite element shell discretizations by use of the “basic shell mathematical model”. Comput Struct 2005;83(1):69-90.
- [21] Theory and Modeling Guide Volume 1:ADINA, Bentley Systems, Inc., ADINA 24.00.01, Section 2.7.3, 2024.
- [22] Ibrahimbegovic A. A novel membrane finite element with an enhanced displacement interpolation. Finit Elel Anal Des 1990;7(2):167-79.
- [23] Irons BM, Razzaque A. Experience with the patch test for convergence of finite elements. In: The mathematical foundations of the finite element method with applications to partial differential equations. Academic Press; 1972. p. 557-87.
- [24] MacNeal RH, Harder RL. A proposed standard set of problems to test finite element accuracy. Finit Elel Anal Des 1985;1(1):3-20.
- [25] Chen XM, Cen S, Long YQ, Yao ZH. Membrane elements insensitive to distortion using the quadrilateral area coordinate method. Comput Struct 2004;82(1):35-54.
- [26] Zouari W, Hammadi F, Ayad R. Quadrilateral membrane finite elements with rotational DOFs for the analysis of geometrically linear and nonlinear plane problems. Comput Struct 2016;173:139-49.
- [27] Hiller JF, Bathe KJ. Measuring convergence of mixed finite element discretizations: an application to shell structures. Comput Struct 2003;81(8):639-54.
- [28] Bathe KJ, Iosilevich A, Chapelle D. An inf-sup test for shell finite elements. Comput Struct 2000;75(5):439-56.
- [29] Lee PS, Bathe KJ. On the asymptotic behavior of shell structures and the evaluation in finite element solutions. Comput Struct 2002;80(3):235-55.
- [30] Ko Y, Lee Y, Lee PS, Bathe KJ. Performance of the MITC3+ and MITC4+ shell elements in widely-used benchmark problems. Comput Struct 2017;193:187-206.
- [31] Bathe KJ, Lee PS, Hiller JP. Towards improving the MITC9 shell element. Comput Struct 2003;81(8):477-89.
- [32] Bathe KJ, Dvorkin EN. On the automatic solution of nonlinear finite element equations. Comput Struct 1983;17(5-6):871-9.
- [33] Wisniewski K. Finite rotation shells: basic equations and finite elements for Reissner kinematics. CIMNE-Springer; 2010.
- [34] Chróscielewski J, Makowski J, Pietraszkiewicz W. Statics and dynamics of multi-segmented shells: nonlinear theory and finite element method. Warsaw: Wydawnictwo IPPT PAN; 2004.
- [35] Bathe KJ. The AMORE paradigm for finite element analysis. Adv Eng Softw 2019; 130:1-13.
- [36] Choi HG, Lee PS. The simplified MITC4+ shell element and its performance in linear and nonlinear analysis. Comput Struct 2024;290:107177.